

# Can 21cm observations discriminate between high-mass and low-mass galaxies as reionization sources?

Ilian T. Iliev<sup>1\*</sup>, Garrelt Mellema<sup>2</sup>, Paul R. Shapiro<sup>3</sup>, Ue-Li Pen<sup>4</sup>, Yi Mao<sup>3</sup>, Jun Koda<sup>3</sup>, Kyungjin Ahn<sup>5</sup>

<sup>1</sup> *Astronomy Centre, Department of Physics & Astronomy, Pevensey II Building, University of Sussex, Falmer, Brighton BN1 9QH, United Kingdom*

<sup>2</sup> *Department of Astronomy & Oskar Klein Centre, Stockholm University, Albanova, SE-10691 Stockholm, Sweden*

<sup>3</sup> *Department of Astronomy, University of Texas, Austin, TX 78712-1083, U.S.A.*

<sup>4</sup> *Canadian Institute for Theoretical Astrophysics, University of Toronto, 60 St. George Street, Toronto, ON M5S 3H8, Canada*

<sup>5</sup> *Department of Earth Science Education, Chosun University, Gwangju 501-759, Korea*

25 December 2021

## ABSTRACT

The prospect of detecting the first galaxies by observing their impact on the intergalactic medium (IGM) as they reionized it during the first billion years leads us to ask whether such indirect observations are capable of diagnosing which types of galaxies were most responsible for reionization. We attempt to answer this by extending the galaxy mass range of our first generation of large-scale radiative transfer simulations of reionization in volumes large enough,  $\geq (100/h\text{Mpc})^3$ , to make statistically meaningful predictions of observable signatures, downward from those above  $10^9 M_\odot$  (high-mass, atomic-cooling halos, or “HMACHs”) to include those between  $10^8$  and  $10^9 M_\odot$  (low-mass, atomic-cooling halos, or “LMACHs”), as well. Previously, we simulated the effects of both HMACHs and LMACHs but only by reducing the box size to  $35/h$  Mpc, too small to apply those simulations to predict observables like the 21-cm background fluctuations. Those simulations showed that LMACHs can make a difference, however. While LMACHs are even more abundant, photoheating suppresses their ability to form stars if they are located inside ionized regions of the IGM, so their contribution starts reionization earlier but tends to saturate over time before it ends. To predict the observables in that case while explicitly tracking the radiation from this full mass range of galaxies, we have had to advance both our N-body and radiative transfer methods substantially, as described here. With this, we perform new simulations in a box 163 Mpc on a side, and focus here on predictions of the 21cm background, to see if upcoming observations are capable of distinguishing a universe ionized primarily by HMACHs from one in which both HMACHs and LMACHs are responsible, and to see how these results depend upon the uncertain source efficiencies.

We find that 21-cm fluctuation power spectra observed by the first generation EoR/21cm radio interferometer arrays should be able to distinguish the case of reionization by HMACHs alone from that by both HMACHs and LMACHs, together. Some reionization scenarios, e.g. one with abundant low-efficiency sources vs. one with self-regulation, yield very similar power spectra and rms evolution and thus can only be discriminated by their different mean reionization history and 21-cm PDF distributions. We find that the skewness of the 21-cm PDF distribution smoothed over LOFAR-like window shows a clear feature correlated with the rise of the rms due to patchiness. This is independent on the reionization scenario and thus provides a new approach for detecting the rise of large-scale patchiness and an independent check on other measurements, regardless of the detailed properties of the sources. The peak epoch of the 21-cm rms fluctuations depends significantly on the beam and bandwidth smoothing size as well as on the reionization scenario and can occur for ionized fractions as low as 30% and as high as 70%. Measurements of the mean photoionization rates are sensitive to the average density of the regions being studied and therefore could be strongly skewed in certain cases. Finally, the simulation volume employed has very modest effects on the results during the early and intermediate stages of reionization, but late-time signatures could be significantly affected.

**Key words:** H II regions: halos—galaxies:high-redshift—intergalactic medium—cosmology:theory—radiative transfer— methods: numerical

arXiv:1107.4772v1 [astro-ph.CO] 24 Jul 2011

## 1 INTRODUCTION

Study of the Epoch of Reionization (EoR) has progressed in recent years in response to a number of new observational developments. The combination of the CMBR data from WMAP (Komatsu et al. 2011; Larson et al. 2011) and ever deeper ground-based observations of high-redshift QSOs, galaxies and GRBs (Ouchi et al. 2010; Kashikawa et al. 2011; Mortlock et al. 2011; Cucchiara et al. 2011; Krug et al. 2011) clearly suggest that the reionization process started early and was quite extended in time. However, observations of the effects of the EoR are just beginning to assemble constraints sufficient to diagnose the conditions which brought it about. Ongoing and upcoming observations are expected to put further, much more stringent constraints on the reionization history. The best constraints are likely to result from redshifted 21-cm experiments with the low-frequency radio interferometers GMRT<sup>1</sup> (Paciga et al. 2011), LOFAR<sup>2</sup> (e.g. Harker et al. 2010), MWA (Lonsdale et al. 2009)<sup>3</sup> and PAPER (Parsons et al. 2010). Additional information will come from Planck satellite (Planck Collaboration et al. 2011) and measurements of the near infrared background with CIBER<sup>4</sup> and AKARI<sup>5</sup>, among others.

The understanding and correct interpretation of these observational results requires detailed modelling. Specific characteristics and features of the observable signatures provide information about different aspects of EoR. One of the central questions is what are the nature, abundances and physical properties of the ionizing sources. Our purpose in this work is to explore how observations of the EoR might diagnose the nature of the reionization sources.

Our first generation of simulations of inhomogeneous reionization combined cosmological N-body simulations of galaxy and large-scale structure formation and the intergalactic density and velocity fields with detailed radiative transfer calculations of the ionizing radiation from every galactic halo whose formation we resolved in a volume large enough to make statistically meaningful predictions of observable consequences of reionization (Iliev et al. 2006; Mellema et al. 2006b; Iliev et al. 2008a, 2007b; Doré et al. 2007; Iliev et al. 2008b; Harker et al. 2009; Ichikawa et al. 2010; Fernandez et al. 2010). These simulations were in comoving boxes of size  $100/h$  ( $= 143$  for  $h = 0.7$  henceforth) Mpc on a side. Previous simulations had been limited to much smaller volumes, too small to serve this purpose. Earlier simulations of smaller volumes, for example, underestimated the width of the time interval for the global transition of the intergalactic medium (IGM) from neutral to ionized (Gnedin 2000; Ricotti et al. 2002; Sokasian et al. 2003; Ciardi et al. 2003), as well as the amplitude of the kSZ fluctuations in the temperature of the CMB from the EOR (Gnedin & Jaffe 2001; Salvaterra et al. 2005). The characteristic size of the intergalactic H II regions during the EOR is expected to reach 10's of Mpc (Furlanetto et al. 2004, 2006a; Friedrich et al. 2011) before they grow large enough to overlap. Any fluctuations introduced by this “patchiness” scale, therefore, require simulation volumes at least this large to model reionization. Moreover, since the first generation of radio observations seeking to detect fluctuations in the brightness temperature of the 21cm background from the EoR have angular resolution of a few arcminutes, a simulation box size in excess of  $\sim 100$  Mpc is necessary to characterize the power spec-

trum, at wavenumbers as small as  $\sim 0.1 \text{ Mpc}^{-1}$  where the initial sensitivity will peak.

Our simulations of a comoving volume  $100/h$  ( $= 143$ ) Mpc on a side were limited, however, by the mass resolution of the N-body simulations, to the direct simulation of galactic halo sources more massive than  $\sim 2 \times 10^9 M_\odot$ . Halo sources are also possible at lower mass if halo gas can radiatively cool below the halo virial temperature to make star formation possible. This includes halos above about  $10^8 M_\odot$ , for which collisional excitation of H atoms can radiatively cool the primordial-composition halo gas since the virial temperature is above  $10^4$  K. We shall refer to these halos between about  $10^8$  and  $10^9 M_\odot$  as low-mass atomic-cooling halos (“LMACHs”), to distinguish them from the halos above  $10^9 M_\odot$ , which we shall call high-mass, atomic-cooling halos (“HMACHs”). LMACHs are more numerous than HMACHs at these epochs, so it might be thought that they would dominate reionization. However, unlike the HMACHs, the LMACHs are vulnerable to the negative feedback effects of photo-heating if they form inside a pre-existing H II region of the IGM, since the pressure of the IGM would then prevent the intergalactic gas from collapsing gravitationally into their dark matter host halos (Efsthathiou 1992; Shapiro et al. 1994; Quinn et al. 1996; Navarro & Steinmetz 1997; Susa & Umemura 2004; Okamoto et al. 2008; Mesinger & Dijkstra 2008). As first emphasized by Shapiro et al. (1994), this limits their contribution to reionization. Halos of even smaller mass than LMACHs would be even more vulnerable to the negative feedback effects of photoionization heating, since they would, in addition to being prevented from capturing intergalactic gas, photoevaporate whatever interstellar gas they had already accumulated before they were engulfed by reionization (Shapiro et al. 2004; Iliev et al. 2005). Before that reionization, however, these minihalos with masses below about  $10^8 M_\odot$ , nevertheless could have formed stars if enough  $\text{H}_2$  molecules were present in them. Since their virial temperatures are below  $10^4$  K, their gas is too cold for collisional excitation and radiative cooling by H atoms, but cooling through the collisionally exciting rotational-vibrational levels of  $\text{H}_2$  is possible. However, these molecules were easily dissociated by the rising UV background of starlight at energies below the ionization threshold of H atoms, an inevitable by-product of the same stars that contributed to reionization. This tends to limit the contribution of minihalos to reionization early in the EoR (Haiman et al. 2000; Ahn et al. 2009). Previous estimates of the minihalo contribution, as a result, assume that this contribution is smaller than that of the LMACHs and HMACHS, so for now, we shall neglect it, although patchiness in the UV background may make them important than one might naively think (Ahn et al. 2009).

To investigate the impact of the LMACHs on reionization and its observable properties by direct radiative transfer simulation of reionization, our first generation of simulations boosted the halo mass resolution in order to resolve all the halos of mass  $10^8 M_\odot$  and above, but sacrificed volume by simulating in a box of size  $37/h$  ( $= 53$  Mpc) on a side (Iliev et al. 2007a). These simulations demonstrated explicitly that reionization in the presence of the LMACHs and their suppression if they formed inside pre-existing H II regions during the EoR was “self-regulated”. The more LMACHs that formed, the more volume and mass of the IGM was ionized, but as this ionized fraction grew, so did the fraction of the total LMACH halo population that formed inside the ionized regions and was suppressed as sources of reionization. This meant that, although the LMACHs dominated the early phase of reionization, their contribution to reionization eventually saturated, and

<sup>1</sup> <http://gmrt.ncra.tifr.res.in/>

<sup>2</sup> <http://www.lofar.org/>

<sup>3</sup> <http://www.mwatelescope.org/>

<sup>4</sup> <http://physics.ucsd.edu/~bkeating/CIBER.html>

<sup>5</sup> <http://irsa.ipac.caltech.edu/Missions/akari.html>

reionization was finished by the HMACHs, whose abundance rose exponentially over time. An observational consequence of importance that is a possible signature of this process was an early onset but late finish for the EoR, as required to explain the high values of electron scattering optical depth reported from WMAP observations of the large-angle fluctuations in the polarization of the CMB. To make further predictions of observable consequences, however, we need to enlarge the volume of these simulations to greater than 100/h Mpc on a side, without losing this enhanced mass resolution necessary to resolve the LMACHs. That is the purpose of the new developments we report in this paper.

To accomplish this goal, it was first necessary to improve and advance both our N-body and radiative transfer methods in order to be able to simulate halo formation with much higher mass resolution and to transfer the ionizing radiation from a much larger number of sources. Toward this end, both codes had to become massively parallel, running on thousands of computing cores, as well as more efficient. These numerical developments are discussed in more detail in § 2 below and in Iliev et al. (2008c).

While the work described here follows naturally from our own previous work as described above, it also differs substantially from other work in the literature to-date involving large-scale radiative transfer simulations of reionization. A full account of that literature is well-beyond the scope of this paper, but we will mention a few points to distinguish the current work. Our N-body simulations resolve all galactic halo sources of  $10^8 M_\odot$  and above, in a comoving box as large as  $114/h = 163$  Mpc on a side. We post-process the density field of the IGM and the galactic halo source populations derived from these N-body simulations by performing a detailed, ray-tracing calculation on a grid of  $256^3$  cells. The simulations described in McQuinn et al. (2007) were based upon post-processing N-body simulations with halo mass resolution above  $10^9 M_\odot$ , in a box  $65.6/h$  Mpc on a side, a volume which is five times smaller than ours, also on a grid of  $256^3$  cells. McQuinn et al. (2007) were, thus, unable to treat explicitly the halo mass range below  $10^9 M_\odot$ , which is subject to suppression by the negative feedback effects of reionization, but they did include a semi-analytical, “subgrid” approximation for the contribution from the unresolved, smaller-mass halos, including some feedback effects. Trac & Cen (2007) considered a  $50/h$  Mpc box, hence, an order of magnitude smaller volume than ours, and  $180^3$  cells for radiative transfer, but their halo mass resolution was similar to ours. They did not consider the feedback effects of reionization on the small-mass galactic halo sources as we do here. Shin et al. (2008) subsequently applied this method to simulate a volume  $100/h$  Mpc on a side ( $2/3$  of our volume), with similar halo mass resolution, on a radiative transfer grid of  $360^3$  cells, to study the structure of the patchy ionization field during the EoR, again without considering feedback and doing only a single simulation, without considering any variation of the (highly uncertain) reionization parameters. Recently, the codes of McQuinn et al. (2007) and Trac & Cen (2007) were compared with each other in Zahn et al. (2011), by comparing results for the ionization fields and 21-cm brightness temperature fluctuation statistics, for reionization simulations advanced part-way through the epoch of reionization, to the 72% ionized point, based upon post-processing a previously-simulated input density field in a box  $100/h$  Mpc on a side, smoothed to a radiative transfer grid with  $256^3$  cells, with halo mass resolution of  $10^8$  solar masses, without any feedback or back-reaction on the halo sources. They also considered a single reionization scenario, with no parameter variation. Finally, Aubert & Teyssier (2010) simulated radiative transfer in several different boxes, as large as  $100/h$  Mpc, by post-processing

a density field and galaxy population derived from separate simulations that combined N-body dynamics and hydrodynamics on a  $1024^3$  grid, but with minimum resolved galaxy masses in that case as large as  $8 \times 10^9 M_\odot$ . No feedback from reionization on galactic sources was considered. While there are other distinctions of detail both between these other simulations and ours and of one from another, we have listed these above to make it clear that our current paper will describe simulations and results which are new, *both* because they are based upon different methodology, applied in greater depth than previously to predict observables like the 21cm background from the EoR, *and* because they are on an unprecedented scale.

The rest of paper is organized as follows. In § 2 we present our codes, numerical methods and simulations. In § 3 we discuss our results on the formation of early cosmic structures. In § 4 we present our results on the basic reionization features, reionization history, integrated electron-scattering optical depth and geometry of ionized patches. The observational signatures derived from our simulations are presented and discussed in § 5. Our conclusions are summarized in § 6. Finally, in Appendix A we present the (physically less realistic) cases of reionization by rare, massive sources, while in Appendix B we discuss the more technical point of the dependence of our results on the Jeans suppression threshold for low-mass sources.

## 2 SIMULATIONS

Our basic methodology has been previously described in Iliev et al. (2006); Mellema et al. (2006b) and Iliev et al. (2007a). Due to the much larger scale of our current simulations compared to our previous ones, both our structure formation and our radiative transfer code had to be significantly developed and re-designed, in particular to allow their massive parallelization on distributed-memory machines. In this section we present our new set of simulations, along with a summary of our methods and parallel code scaling to large number of computing cores.

### 2.1 N-body simulations

We start by performing very high resolution N-body simulations of the formation of high-redshift structures. We use the CubeP<sup>3</sup>M N-body code<sup>6</sup> which evolved from the particle-mesh (PM) code PMFAST Merz et al. (2005). In CubeP<sup>3</sup>M several important new features were introduced in comparison with these previous codes. The first one is the addition of a short-range direct particle-particle force, making it a  $P^3M$  (particle-particle-particle-mesh) code. This significantly improves its spatial resolution and accuracy at small scales compared to PM codes. A second important new development is that CubeP<sup>3</sup>M is now a massively parallel code which can run efficiently on either distributed- or shared-memory machines. This is achieved through cubical equal-volume domain decomposition and a hybrid MPI and OpenMP approach (see (Iliev et al. 2008c) for more details). CubeP<sup>3</sup>M scales well (with ‘weak’ scaling, whereby the execution time rises proportionally to the problem size) up to thousands of processors, as shown in Fig. 1 (left) and has to date been run on up to 21,976 computing cores, following up to  $5488^3$  particles (Iliev et al. 2010). These

<sup>6</sup> <http://www.cita.utoronto.ca/mediawiki/index.php/CubePM> for description of the code see also (Iliev et al. 2008c).

**Table 1.** N-body simulation parameters. Background cosmology is based on the WMAP 5-year results.

boxsize	$N_{part}$	mesh	spatial resolution	$m_{particle}$	$M_{halo,min}$
37 $h^{-1}$ Mpc	1024 <sup>3</sup>	2048 <sup>3</sup>	1.81 kpc/h	$5.05 \times 10^6 M_{\odot}$	$1.01 \times 10^8 M_{\odot}$
64 $h^{-1}$ Mpc	1728 <sup>3</sup>	3456 <sup>3</sup>	1.85 kpc/h	$5.44 \times 10^6 M_{\odot}$	$1.09 \times 10^8 M_{\odot}$
74 $h^{-1}$ Mpc	2048 <sup>3</sup>	4096 <sup>3</sup>	1.81 kpc/h	$5.05 \times 10^6 M_{\odot}$	$1.01 \times 10^8 M_{\odot}$
114 $h^{-1}$ Mpc	3072 <sup>3</sup>	6144 <sup>3</sup>	1.86 kpc/h	$5.47 \times 10^6 M_{\odot}$	$1.09 \times 10^8 M_{\odot}$

scaling tests were run on the Texas Advanced Computing Center (TACC) computer, *Lonestar*, and on the currently-available portion of the European Petascale computer under development in France, *Curie*, at CEA, part of the Partnership for Advanced Computing in Europe (PRACE). Our results show almost perfect scaling of CubeP<sup>3</sup>M, within 3% of the ideal one (dashed line), for up to 2,048 cores.

We performed a series of N-body cosmic structure formation simulations (summarized in Table 1) with increasing simulation box size, from 37  $h^{-1}$ Mpc (53 Mpc) up to 114  $h^{-1}$ Mpc (163 Mpc), but all with a fixed spatial and mass resolution. These N-body simulations were run on a range of core number from 256 (1024<sup>3</sup> particles) up to 2048 cores (3072<sup>3</sup> particles). The force smoothing length is fixed to 1/20 of the mean inter-particle spacing, or 1.8  $h^{-1}$  kpc. The largest of these simulations follows a volume which is 50% larger than the largest structure formation simulation performed previously at similar resolution.

The N-body simulations required between 4,100 (for 1024<sup>3</sup> particles) and 159,000 (for 3072<sup>3</sup> particles) computing hours (computing cores  $\times$  wall-clock hours) on the TACC computer *Ranger* (SunBlade x6420 with AMD x86 64 Opteron Quad Core, 2.3 GHz, 9.2 GFlops per core Barcelona processors and Infiniband networking). The particle mass is  $5 \times 10^6 M_{\odot}$ , which guarantees that all atomically-cooling halos ( $M > 10^8 M_{\odot}$ ) are resolved with at least 20 particles. We use a spherical overdensity halo finder with overdensity parameter fixed to 178 of mean density (Note that  $\bar{\rho}_M \neq \rho_{crit}$  except for very high redshift. The series of N-body simulations with an increasing size allowed us to test the convergence of our results with computational box size.

The background cosmology is based on WMAP 5-year data combined with constraints from baryonic acoustic oscillations and high-redshift supernovae ( $\Omega_M = 0.27$ ,  $\Omega_{\Lambda} = 0.73$ ,  $h = 0.7$ ,  $\Omega_b = 0.044$ ,  $\sigma_8 = 0.8$ ,  $n = 0.96$ ). The linear power spectrum of density fluctuations was calculated with the code CAMB (Lewis et al. 2000). Initial conditions were generated using the Zel'dovich approximation at sufficiently high redshift ( $z_i = 300$ ) to ensure against numerical artifacts (Crocce et al. 2006).

## 2.2 Radiative transfer simulations

The radiative transfer simulations are performed with our code C<sup>2</sup>-Ray (Conservative Causal Ray-Tracing) (Mellema et al. 2006a). The method is explicitly photon-conserving in both space and time for individual sources and approximately (to a good approximation) photon-conserving for multiple sources, which ensures correct tracking of ionization fronts without loss of accuracy, independent of the spatial and time resolution, with corresponding great gains in efficiency. The code has been tested in detail against a number of exact analytical solutions (Mellema et al. 2006a), as well as

in direct comparison with a number of other independent radiative transfer methods on a standardized set of benchmark problems (Iliev & et al. 2006; Iliev et al. 2009). The ionizing radiation is ray-traced from every source to every grid cell using the short characteristics method, whereby the neutral column density between the source and a given cell is given by interpolation of the column densities of the previous cells which lie closer to the source, in addition to the neutral column density through the cell itself. The contribution of each source to the local photoionization rate of a given cell is first calculated independently, after which all contributions are added together and a nonequilibrium chemistry solver is used to calculate the resulting ionization state. Ordinarily, multiple sources contribute to the local photoionization rate of each cell. Changes in the rate modify the neutral fraction and thus the neutral column density, which in turn changes the photoionization rates themselves (since either more or less radiation reaches the cell). An iteration procedure is thus called for in order to converge to the correct, self-consistent solution. While our basic methodology remains essentially as described in Mellema et al. (2006a), our C<sup>2</sup>-Ray code has been thoroughly re-written in Fortran 90, made more flexible and modular and parallelized for distributed-memory machines. In terms of parallelization strategy, due to the causal nature of the ray-tracing procedure (i.e. the state of each cell can be calculated only after all previous cells, closer to the source are done) it is not possible to employ domain decomposition (except for a limited one, into octants, see below), although other approaches exist which seek ways to overcome this limitation (Nakamoto et al. 2001; Rijkhorst et al. 2006). Instead, the main code loop over the sources of ionizing radiation is done in massively parallel fashion. Each MPI node has a copy of the density field and receives a number of sources whose radiation is to be traced through the grid. For the large-scale cosmological reionization problem there are typically hundreds of thousands to millions of sources, thus our code scales well up to tens of thousands of cores at least (see next section). For problems with (relatively) low number of ionizing sources such parallelization strategy would be inefficient, but such problems are not sufficiently computationally-intensive to require such massive parallelization and could, instead, be solved on a smaller number of nodes, or even in serial. A similar situation occurs for the initial steps of the simulations presented below, when the cosmological structure formation is not yet much advanced, thus only a few to few tens of halos form. However, their number increases exponentially over time, quickly reaching thousands, and then tens and hundreds of thousands. We therefore start our simulations on a small number of cores (typically 32), raising to thousands of cores as more sources form.

As mentioned above, a limited domain decomposition onto octants is possible for our method, since those are independent of each other within the short-characteristic ray-tracing framework.

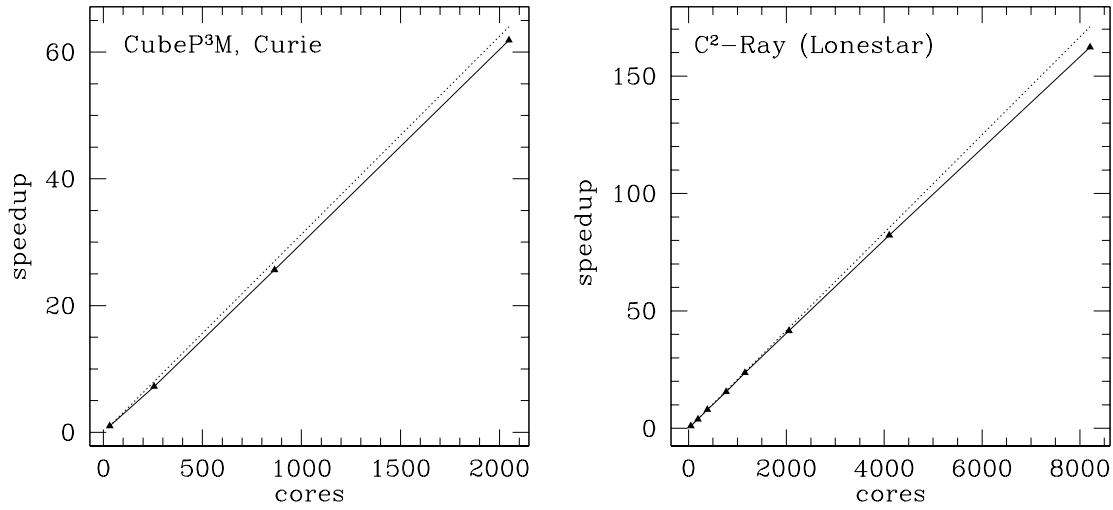


**Figure 1.** (a)(left) Scaling of the CubeP3M code. Plotted are the code speedup vs. the number of computational cores used. Both quantities are normalized to the smallest run in each case. (b)(right) Scaling of the C2-Ray code. Plotted are the code speedup vs. the number of computational cores used, again normalized to the smallest of the three runs compared. Dashed line indicates the ideal weak scaling for each case.

**Table 2.** Reionization simulation parameters and global reionization history results. All runs use background cosmology based on the WMAP 5-year results.

label	run	boxsize [cMpc]	$g_\gamma(f_\gamma)^3$ HMACH	$g_\gamma(f_\gamma)$ LMACH	mesh	supp.	min source [ $M_\odot$ ]	min unsupp. halo [ $M_\odot$ ]	$\tau_{\text{es}}$	$z_{10\%}$	$z_{50\%}$	$z_{90\%}$	$z_{\text{ov}}$
L1	163Mpc-g8.7-130S	163	8.7 (10)	130 (150)	256 <sup>3</sup>	yes	10 <sup>8</sup>	10 <sup>9</sup>	0.080	13.3	9.4	8.6	8.3
L2	163Mpc-g1.7-8.7S	163	1.7 (2)	8.7 (10)	256 <sup>3</sup>	yes	10 <sup>8</sup>	10 <sup>9</sup>	0.058	9.9	7.6	6.9	6.7
L3	163Mpc-g21.7-0	163	21.7 (25)	0 (0)	256 <sup>3</sup>	no	$2.2 \times 10^9$	$2.2 \times 10^9$	0.070	10.3	9.1	8.6	8.4
S1	53Mpc-g8.7-130S	53	8.7 (10)	130 (150)	256 <sup>3</sup>	yes	10 <sup>8</sup>	10 <sup>9</sup>	0.084	13.6	9.8	8.9	8.5
S2	53Mpc-g1.7-8.7S	53	1.7 (2)	8.7 (10)	256 <sup>3</sup>	yes	10 <sup>8</sup>	10 <sup>9</sup>	0.059	10.0	7.7	6.9	6.7
S3	53Mpc-g8.7-130	53	8.7 (10)	130 (150)	256 <sup>3</sup>	no	10 <sup>8</sup>	10 <sup>8</sup>	0.131	15.6	13.9	13.2	12.9
S4	53Mpc-g0.4-5.3	53	0.35 (0.4)	5.3 (6)	256 <sup>3</sup>	no	10 <sup>8</sup>	10 <sup>8</sup>	0.078	11.7	9.7	8.9	8.6
S5	53Mpc-g10.4-0	53	10.4 (12)	0	256 <sup>3</sup>	no	10 <sup>9</sup>	10 <sup>9</sup>	0.071	10.5	9.1	8.5	8.3
S6	53Mpc-g8.7-130S9	53	8.7 (10)	130 (150)	256 <sup>3</sup>	yes <sup>2</sup>	10 <sup>8</sup>	10 <sup>9</sup>	0.111	14.9	12.6	10.7	9.5
S7	53Mpc-g8.7-130S5	53	8.7 (10)	130 (150)	256 <sup>3</sup>	yes <sup>2</sup>	10 <sup>8</sup>	10 <sup>9</sup>	0.089	13.9	10.1	9.0	8.6
S8	53Mpc-uvS-1e9	53	variable <sup>1</sup>	0	256 <sup>3</sup>	no	10 <sup>9</sup>	10 <sup>9</sup>	0.084	13.7	9.7	8.9	8.5
S9	53Mpc-uvS-1e10	53	variable <sup>1</sup>	0	256 <sup>3</sup>	no	10 <sup>10</sup>	10 <sup>10</sup>	0.080	12.2	9.8	8.9	8.5

<sup>1</sup> see Figure A1 and discussion in Appendix A. <sup>2</sup> employing a different suppression criterion, see Appendix B.

<sup>3</sup>  $f_\gamma$  is related to  $g_\gamma$  by Eqn. (2) with  $\Delta t = 11.53$  Myrs.

We use this to (optionally) improve the memory efficiency of the code by doing the grid octants in parallel within each MPI node using OpenMP multi-threading. This way each MPI node needs only one copy of the grid, which is shared amongst the cores within the node.

The radiative transfer problem size scales proportionally to both the grid size and the number of sources. Results, shown in Figure 1 (right) demonstrate almost perfect scaling, within  $\sim 10\%$  from the ideal one, for up to 8,192 cores.

The N-body simulations discussed above provide us with the

spatial distribution of cosmological structures and their evolution in time. We then use this information as input to a full 3D radiative transfer simulations of the reionization history, as follows. We saved series of time-slices, both particle lists and halo catalogues from redshift 50 down to 6, uniformly spaced in time, every  $\Delta t = 11.53$  Myr, a total of 76 slices. Based on the particle distribution at each redshift we used SPH-style smoothing scheme using the nearest neighbours (to be described in detail in a companion paper, in prep.) to produce regular-grid density and bulk velocity fields at the radiative transfer resolution of 256<sup>3</sup> cells.

All identified halos are potential sources of ionizing radiation, with a photon production rate per Myr,  $\dot{N}_\gamma$ , proportional to their mass,  $M$ :

$$\dot{N}_\gamma = \frac{f_\gamma M \Omega_b}{\Delta t \mu \Omega_0 m_p}, \quad (1)$$

where  $m_p$  is the proton mass and  $f_\gamma = f_{\text{esc}} f_\star N_\star$  is an ionizing photon production efficiency parameter which includes the efficiency of converting gas into stars,  $f_\star$ , the ionizing photon escape fraction from the halo into the IGM,  $f_{\text{esc}}$  and the number of ionizing photons produced per stellar atom,  $N_\star$ . The latter parameter depends on the assumed IMF for the stellar population and varies between 4,000 and  $\sim 100,000$ . Halos were assigned different luminosities according to whether their mass was above (“large sources”) or below (“small sources”)  $10^9 M_\odot$  (but above  $10^8 M_\odot$ , the minimum resolved halo mass). Low-mass sources are assumed to be suppressed within ionized regions (for ionization fraction higher than 10%), through Jeans-mass filtering, as discussed in Iliev et al. (2007a).

We note that while previously we used the factor,  $f_\gamma$ , to characterize the source efficiencies, here we define a slightly different factor,  $g_\gamma$ , that is given by

$$g_\gamma = f_\gamma \left( \frac{10 \text{ Myr}}{\Delta t} \right) \quad (2)$$

where  $\Delta t$  is the time between two snapshots from the N-body simulation. The new factor  $g_\gamma$  has the advantage that it is independent of the length of the time interval between the density slices, and as such it allows a direct comparison between runs with different  $\Delta t$ . For reader’s convenience we listed the values of both parameters in Table 2. We also note that the specific numerical values of the efficiency parameters are strongly dependent on the background cosmology adopted and the minimum source halo mass. Therefore, parameter values for simulations based on different underlying cosmology and resolution should not be compared directly, but would require a cosmology and resolution-dependent conversion coefficients to achieve the same reionization history.

Our full simulation notation reads *Lbox\_gI\_J(S)(K)* (the bracketed quantities are listed only when needed), where ‘*Lbox*’ is the simulation box size in Mpc, ‘*I*’ and ‘*J*’ are the values of the  $g_{\text{gamma}}$  factor for HMACHs and LMACHs, respectively, the symbol ‘*S*’ means that the small sources are suppressed within already-ionized regions and ‘*K*’ indicated the ionized fraction threshold for a given radiative transfer cell above which this suppression occurs for halos residing in that cell, which is 0.1 if not listed explicitly and raised to 0.9 or 0.5 for cases  $K = 9$  and  $K = 5$ , respectively (see below for details). For example, 53Mpc\_g8.7\_130S indicates that large sources have an efficiency  $g_\gamma = 8.7$ , while small sources have an efficiency  $g_\gamma = 130$  and are suppressed in ionized regions.

We have performed series of radiative transfer simulations with varying underlying assumptions about the source efficiencies and the suppression conditions imposed on the low-mass sources, as summarized in Table 2. For our radiative transfer simulations we use the data from the largest N-body box,  $114/h = 163$  Mpc, and the smallest one of these,  $37/h = 53$  Mpc. The former volume is sufficiently large to faithfully represent the reionization observables, while the latter one affords much faster and computationally cheaper simulations, which allows us to explore a wider parameter space. These two very different computational volumes also allow us to investigate resolution effects and evaluate which features of reionization and observable signatures are sensitive to the box size and which are less so. We label all runs by a short label (listed in

the first column of Table 2) for more compact notation. Large-box runs are labelled L1-L3, while small-box ones are labelled S1-S9.

Our fiducial runs, to which all the others will be compared are 163Mpc\_g8.7\_130S (L1) and the companion small-box one with same source efficiencies, 53Mpc\_g8.7\_130S (S1). These parameters yield a relatively early overlap and high electron scattering optical depth. The second set of simulations, 163Mpc\_g1.7\_8.7S (L2) and 53Mpc\_g1.7\_8.7S (S2) are in the opposite limit, which assumes considerably lower efficiencies for both types of sources and as a consequence serves as a model for a late-overlap, extended, more photon-poor reionization scenario. These two cases are designed to roughly bracket the range of observationally-allowed reionization scenarios.

Our third large-box simulation, 163Mpc\_g21.7\_0 (L3) is equivalent to our previous large-box simulations without self-regulation presented in (Iliev et al. 2008a), except for the updated background cosmology and the source photon production efficiencies, adjusted here to yield the same overlap epoch as our fiducial case L1. Therefore, L1 and L3 share the underlying density structures and sources (apart from the different minimum mass cutoffs) and hence a head-to-head comparison yields the effects of the presence of low-mass sources and Jeans-mass filtering.

The rest of our cases, S3 to S9, test various aspects of the reionization source modelling. Simulation S3 is an extreme case which has the same source efficiencies as our fiducial case L1, but assumes no suppression occurs. Naturally, this results in a very early reionization and very high integrated optical depth,  $\tau_{\text{es}} = 0.131$ , which is well outside the WMAP5  $1 - \sigma$  range of  $\tau_{\text{es}} = 0.084 \pm 0.016$ . Simulation 53Mpc\_g0.4\_5.3 (S4) is again without suppression, but here we tuned down the efficiencies of both types of sources so as to achieve approximately the same overlap epoch as in our fiducial case L1. In simulation 53Mpc\_g10.4\_0 (S5) we assume that there are no low-mass,  $M < 10^9 M_\odot$  sources at all and we adjust the photon efficiency of the remaining sources to again reach overlap at roughly the same epoch as in the fiducial case.

Additionally, we consider two scenarios which have exactly the same time-dependent ionizing photon emissivity (and therefore almost identical reionization history) as our fiducial case S1, but with higher minimum source mass of  $10^9 M_\odot$  (53Mpc\_uvS\_1e9; S8) and  $10^{10} M_\odot$  (53Mpc\_uvS\_1e10; S9). The fixed ionizing photon emissivity results in unphysically high early source luminosities and we consider them primarily in order to illustrate the effect of re-distributing the full luminosity of all sources over the massive ones only, similar to the models adopted in some recent work (Thomas et al. 2009; Baek et al. 2009). These simulations and some illustrative results from them are discussed in Appendix A.

Finally, in order to evaluate the robustness of our source suppression model, we consider two more scenarios, 53Mpc\_g8.7\_130S9 (S6) and 53Mpc\_g8.7\_130S5 (S7), whereby we raise the ionization threshold for low-mass source suppression to  $x_{\text{threshold}} = 0.9$  and 0.5, respectively, from our fiducial threshold of  $x_{\text{threshold}} = 0.1$ . Since this is a more technical study we present its results separately, in Appendix B.

The radiative transfer simulations presented in this work typically required  $\sim 0.5 - 1$  million computing hours (163 Mpc boxes) and  $\sim 10 - 30$  thousand computing hours (53 Mpc boxes), depending on the specific set of source parameters we adopted.



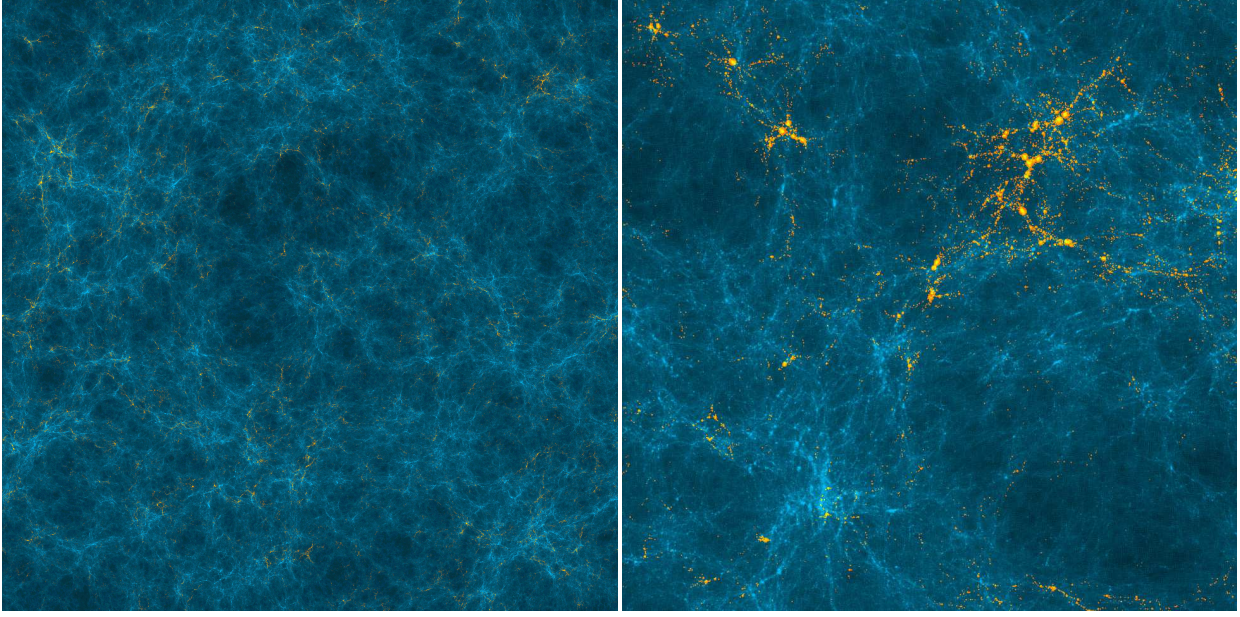


**Figure 2.** (left) Slice of the Cosmic Web at redshift  $z = 6$  from our CubeP<sup>3</sup>M simulation with 3072<sup>3</sup> particles (29 billion) on a 6144<sup>3</sup> fine grid in a comoving volume of 163 Mpc on a side. Shown are the dark matter density (blue) and halos (in actual size; yellow). Image resolution is 6144 × 6144, the slice is 1/ $h$  Mpc thick. (right) Zoomed-up region (25.76×25.76 Mpc) of the same image.

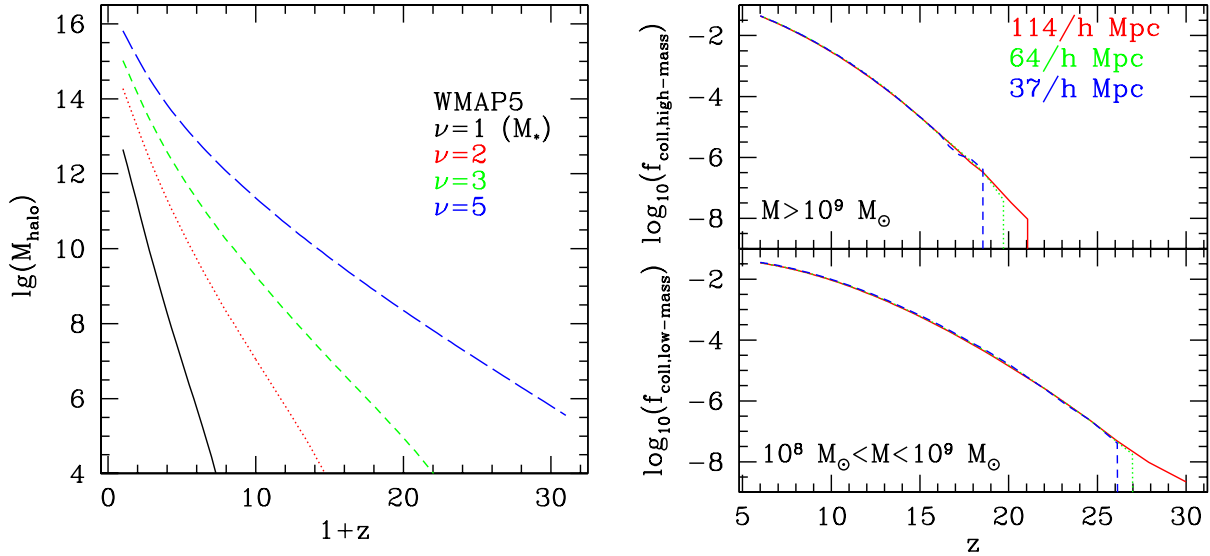


**Figure 3.** (left) Halo abundances for  $\nu = \delta_c D_+ / \sigma(0, M) = 1$  ( $M_*$ ; black, solid), 2 (red, dotted), 3 (green, short-dashed), and 5 (blue, long-dashed). (right) Collapsed fraction of HMACHs (top) and LMACHs (bottom) halos.

### 3 RESULTS: EARLY STRUCTURE FORMATION

In Figure 2 (left: full box, right: zoomed sub-volume) we show a slice of the density field and halos at redshift  $z = 6$  from our 114  $h^{-1}$  Mpc (163 Mpc), 3072<sup>3</sup>-particle N-body simulation. The structure formation is already well-advanced and strongly nonlinear at sub-Mpc scales. The very first resolved ( $M_{\text{halo}} > 10^8 M_\odot$ ) halo in this volume forms at  $z = 31$ , while the first insuppressible halo ( $M_{\text{halo}} > 10^9 M_\odot$ ) forms at  $z = 21$ . By  $z = 6$  there are over 20.5 million collapsed halos, of which  $\sim 18.7$  million low-mass ( $M_{\text{halo}} < 10^9 M_\odot$ ) halos and  $\sim 2$  million high-mass ( $M_{\text{halo}} >$

$10^9 M_\odot$ ) halos. The halos are strongly clustered at all times, more so going to higher redshifts, when they are ever rarer. The halo abundances are usually described in terms of  $\nu = \delta_c D_+ / \sigma(0, M)$ , where  $\delta_c$  is the linear density contrast corresponding to the moment of collapse of a top-hat density perturbation,  $\sigma(0, M)$  is the present variance of the density fluctuations corresponding to the mass scale  $M$ , and  $D_+$  is the growth factor of the density fluctuations. The halo masses corresponding to  $\nu = 1$  (most common,  $M_*$ , halos),  $\nu = 2, 3$ , (rare halos) and  $\nu = 5$  (extremely rare halos) are shown in Figure 3 (left). Clearly, before  $\sim 6$ , within the redshift range of

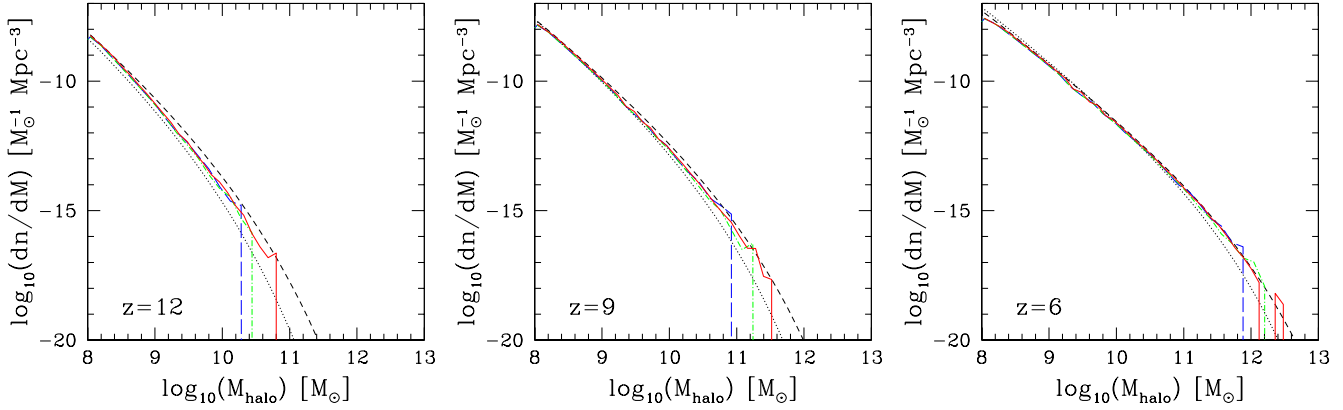


**Figure 4.** Simulated halo mass function at high- $z$  derived from 114/ $h$  Mpc box (solid, red), 74/ $h$  Mpc box (dot-dashed, green), 37/ $h$  Mpc box (long-dashed, blue) at (left to right)  $z = 12$ , 9 and 6. Also shown are the Press-Schechter (dotted, black) and Sheth-Tormen (short-dashed, black) analytical mass functions.

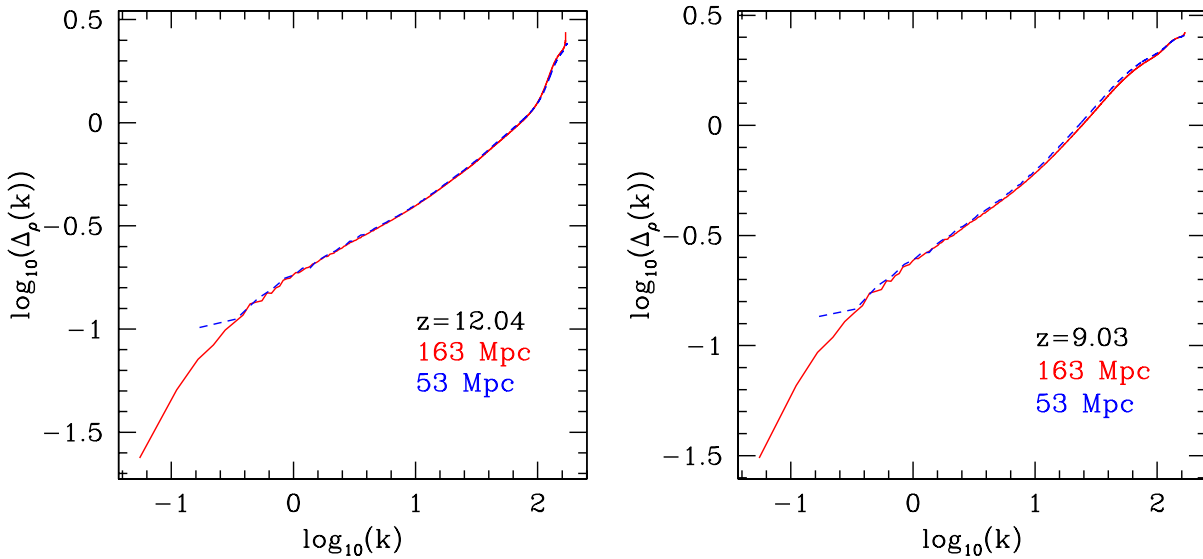


**Figure 5.** The power spectra of the density fields,  $\Delta_\rho = (k^3 P(k)/2\pi^2)^{1/2}$ , for the 114/ $h = 163$  Mpc box run (red, solid) and the 37/ $h = 53$  Mpc box run (blue, dashed) at redshifts  $z = 12$  (left) and  $z = 9$  (right).

interest here, there are no  $1 - \sigma$  halos at all and all halos are rare. Atomically-cooling halos are  $2 - 3 - \sigma$  at the low end of the redshift interval and as rare as  $5 - \sigma$  at early times. The evolution of the collapsed fractions in high-mass and low-mass halos is shown in Fig 3 (right). The collapsed fractions start very low and rise exponentially at early times when the halos are very rare. The collapsed fraction in low-mass halos reaches  $10^{-3}$  and 1% at  $z = 14$  and  $z = 9.8$ , respectively. After that point it starts to level off as low-mass halos start to become less rare ( $2 - \sigma$  or less) and their collapsed fraction reaches 3.4% by  $z = 6$ . The collapsed fraction in high-mass halos rises steeply all the way to  $z = 6$ , eventually reaching 4.25%. There is only a modest departure from the exponential growth, reflecting the fact that they remain quite rare throughout this period. The simulation volume has essentially no effect on the derived collapsed fractions, indicating numerical convergence on that quantity at fixed mass resolution. The only exception to this is at very early times ( $z > 26$  for the low-mass halos and  $z > 17$  for the high-

mass ones) the corresponding halo populations are so rare ( $\sim 5 - \sigma$  in each case) that Poisson noise (i.e. cosmic variance, due to the smaller volume) affects the results. For example, the first resolved halos form at  $z = 31$  in the  $114 h^{-1}$  Mpc box, but only at  $z = 26$  in the  $37 h^{-1}$  Mpc box. As soon as there is sufficient statistics for any given volume the collapsed fractions converge.

The halo mass functions derived from our simulations are shown in Figure 4 for a range of redshifts,  $z = 12 - 6$ , along with the Press-Schechter (PS; Press & Schechter 1974) and Sheth-Tormen (ST; Sheth & Tormen 2002) analytical mass functions. The halo abundancies at all redshifts fall between those two analytical predictions. PS always under-predicts the abundances of massive, rare halos, while ST over-predicts them. With time ST becomes a better match to the numerical results. This broadly agrees with previous results on the high-redshift mass functions (Iliev et al. 2006; Reed et al. 2007; Lukić et al. 2007).

In Fig. 5 we plot the total matter density field power spectra



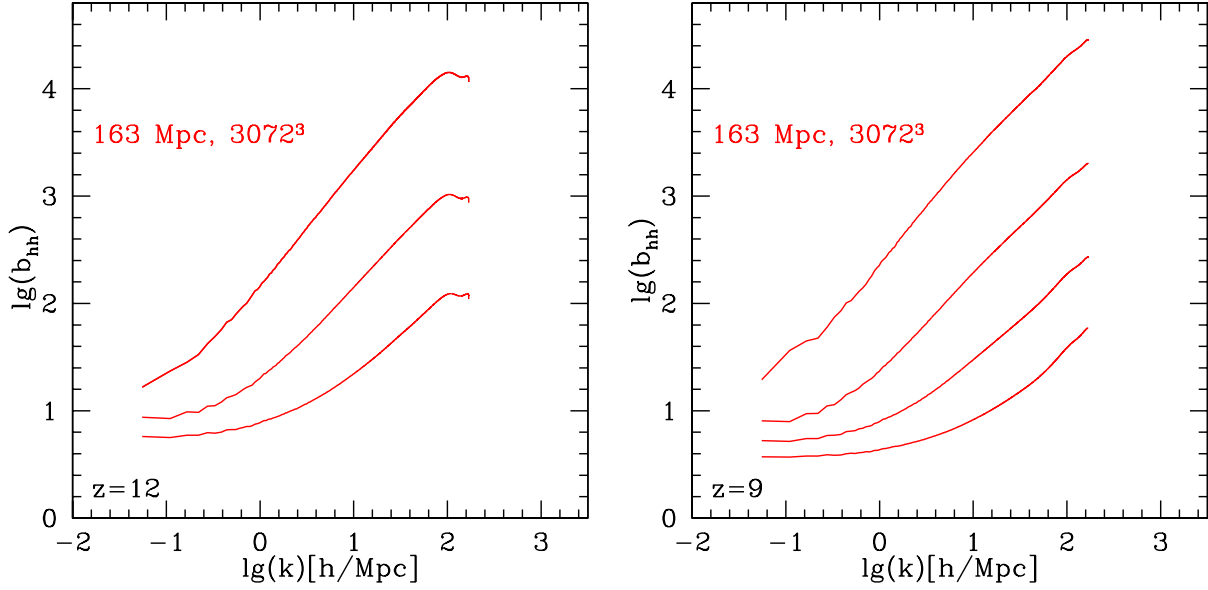


**Figure 6.** The halo bias,  $b_{hh} = \Delta_{hh}/\Delta_\rho$ , for the  $114/h = 163$  Mpc box run (red, solid) at redshifts  $z = 12.04$  (left) and  $z = 9.03$  (right). Lines are for halos binned by decades of mass (bottom to top curve)  $10^8 M_\odot < M_{\text{halo}} < 10^9 M_\odot$ ,  $10^9 M_\odot < M_{\text{halo}} < 10^{10} M_\odot$ ,  $10^{10} M_\odot < M_{\text{halo}} < 10^{11} M_\odot$ , and  $10^{11} M_\odot < M_{\text{halo}} < 10^{12} M_\odot$ .

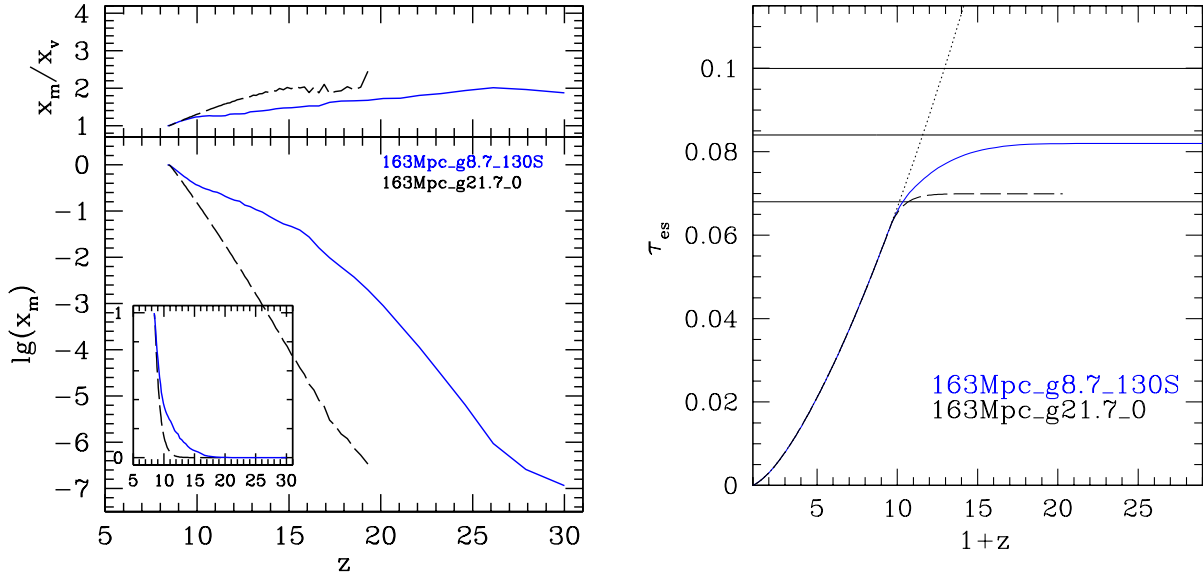


**Figure 7.** The effect of self-regulation on the reionization history and integrated electron-scattering optical depth: (left) Mass-weighted reionization histories (bottom) and the ratio of the mean mass-weighted and volume ionized fractions,  $x_m/x_v$  (top) for our fiducial self-regulated case, L1 (blue, solid) and the corresponding non-selfregulated case with same overlap epoch, L3 (black, long-dashed). The computational box size is 163 Mpc in both cases. Inset shows the same reionization histories in linear scale. (right) The corresponding electron scattering optical depth,  $\tau_{\text{es}}(z)$  integrated from redshift 0 to redshift  $z$  for the same two simulations. Horizontal lines indicate the mean and  $1-\sigma$  band derived from the WMAP 5-year data, while the dotted line shows the value of  $\tau_{\text{es}}$  for a fully-ionized universe.

$\Delta_\rho = (k^3 P(k)/2\pi^2)^{1/2}$  at two representative redshifts for our largest (114 Mpc/h) and smallest (37 Mpc/h) boxes. Power spectra were calculated by interpolating the N-body particles using a cloud-in-cell scheme onto the fine grid of the CubeP<sup>3</sup>M code, with  $6144^3$  and  $2048^3$  cells, respectively. There is a close agreement between the two cases, apart from the expected variance at scales

close to the box size. This shows that there is no missing density fluctuation power in the small box, except for the scales at or above the box size.

Finally, in Figure 6 we show the halo-halo bias, calculated as the ratio of the halo autocorrelation power spectrum divided by the density field one, i.e.  $b_{hh} = \Delta_{hh}/\Delta_\rho$ . This measures the cluster-

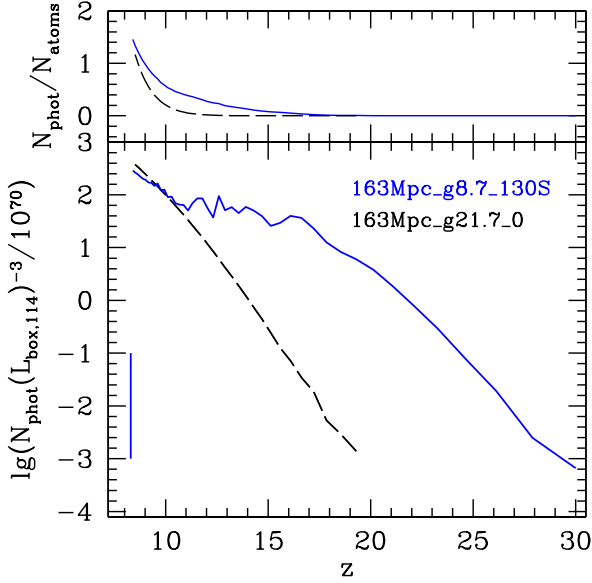


**Figure 8.** (bottom) Number of ionizing photons emitted by all active sources in the computational volume per timestep and (top) cumulative number of photons per total gas atom released into the IGM. Notation is the same as in Fig. 7. The vertical line marks the overlap redshift ( $z(x_m = 0.99)$ ) for each case.

ing of the dark matter halos with respect to the underlying matter density field at redshifts  $z = 12$  and  $9$ , roughly corresponding to early and advanced stages of reionization. Because of the relative rarity of all halos studied here, their clustering is quite strong, particularly at the smallest resolved scales ( $k \sim 100 h/\text{Mpc}$ ), where it is of order 100 for the lowest mass halos and is as high as  $\sim 10^4$  for the most massive halos. At these small scales the bias is strongly nonlinear. At large scales the bias factors asymptote to a (mass-dependent) constant - the large-scale linear bias (Mo & White 1996). The transition between the large-scale linear bias and the nonlinear one occurs around  $k \sim 1$  for the lowest-mass halos at  $z = 9$ , rising to  $k \sim 0.1 - 0.5$  for the larger halos and/or higher redshifts. The largest, rarest halos ( $M > 10^{11} M_\odot$  at  $z = 12$ ,  $M > 10^{11} M_\odot$  at  $z = 9$ ) show a roughly linear log-log  $b(k)$  relation and never asymptote to the linear bias value within the  $k$ -range covered in our simulation.

## 4 RESULTS: BASIC FEATURES OF THE SELF-REGULATED REIONIZATION

### 4.1 The effects of self-regulation

We start by comparing our fiducial simulation L1 against the simulation L3, equivalent to our previous large-box simulations without LMACHs and their self-regulation (Iliev et al. 2008a). The resulting reionization histories and integrated electron-scattering optical depths are shown in Figure 7. As expected, the self-regulated model yields a much more gradual and extended reionization history, which starts with the formation of the first atomically-cooling halo sources at  $z \sim 31$  vs. the much later start, at  $z \sim 20$  in L3, due to the much larger, rarer sources in the latter case, which accordingly form later. The exponential rise in the numbers of the high-mass sources yields a steep, power-law like reionization history (reasonably well-fit by  $\lg(x_m) \approx -1.226z + 10.41$  for  $x_m > 0.03$ ,

rising somewhat steeper than this earlier on) when it is driven solely by those sources, while in the self-regulated case the steep initial rise becomes much more gradual when the self-regulation first kicks in, around  $z \sim 16$ , when the efficient low-mass sources are massively suppressed and thereby gradually give way to the less efficient high-mass ones which come to dominate at the latter stages of reionization. However, we note that even with self-regulation the reionization history remains monotonic and no plateaus, let alone double reionization, ever occur. The mass-weighted over volume ionized fraction (upper panel) is always lower in the self-regulated case, indicating that reionization has less pronounced inside-out character, i.e. ionized regions are less correlated with the highest density peaks in this case since reionization is driven by wider range of sources, including low-mass, less biased ones. The integrated electron-scattering optical depth (Figure 7, right) is significantly boosted by the presence of low-mass sources, by about 0.01 overall, most of it due to the early stages of reionization. For the particular source efficiencies we have chosen here both optical depths fall within the  $1-\sigma$  interval given by the WMAP 5-year data, albeit the value for the self-regulated fiducial case is very close to the central value, while the  $\tau_{\text{es}}$  for the L3 case is at the low  $1-\sigma$  limit.

These reionization histories are a direct consequence of the overall number of ionizing photons emitted by all active sources, shown in Figure 8. In the case L3 where no source suppression occurs the number of photons emitted per timestep simply rises proportionally to the halo collapsed fraction, roughly exponentially. In contrast, in the fiducial self-regulated case L1 the initial exponential rise is halted around redshift  $z \sim 16$  and rises very slowly (and moderately non-monotonically) until  $z \sim 11$ , at which point sufficient number of high-mass, non-suppressible sources form to allow them to take over the evolution, while the low-mass sources become highly suppressed. Therefore, similarly to our earlier results in Iliev et al. (2007a) the late phase of reionization and overlap epoch,  $z_{\text{ov}}$ , are dominated by HMACHs, while the LMACHs dominate the early phase of reionization and provide a significant boost to the electron-scattering optical depth,  $\tau_{\text{es}}$ . Ultimately, by overlap in both simulations L1 and L3 there are 1.2-1.6 ionizing photon per atom emitted, slightly more in the self-regulated case due to its more extended reionization history which yields more recombinations per atom.

### 4.2 The effects of source efficiencies and box size

The reionization histories derived from our suite of simulations are shown in Fig. 9. The reionization history is monotonic in all cases, although due to the self-regulation the slope of the curves can vary significantly and in particular can become almost horizontal for short periods of time when the Jeans mass filtering compensates for the rise in source numbers. The exact redshifts at which certain reionization milestones, 10%, 50% and 90% by mass, are reached are listed in Table 2. We also list there the epochs when final overlap, which we define as the time when  $x_m = 0.99$ , i.e. at least 99% of the mass is ionized, is reached in each case.

Our large-volume, self-regulated simulations L1 and L2 (Fig. 9, left panels) have reionization histories which are very similar to each other, but offset by  $\Delta z \sim 2$ . Overlap is reached at  $z = 8.3$  (6.7) in L1 (L2), corresponding to early (extended) reionization scenarios. The integrated electron scattering optical depth for L1 is  $\tau_{\text{es}} = 0.080$  for the early reionization case, well within the current WMAP5  $1-\sigma$  constraints. The corresponding value for the low-efficiency, extended reionization scenario L2 is

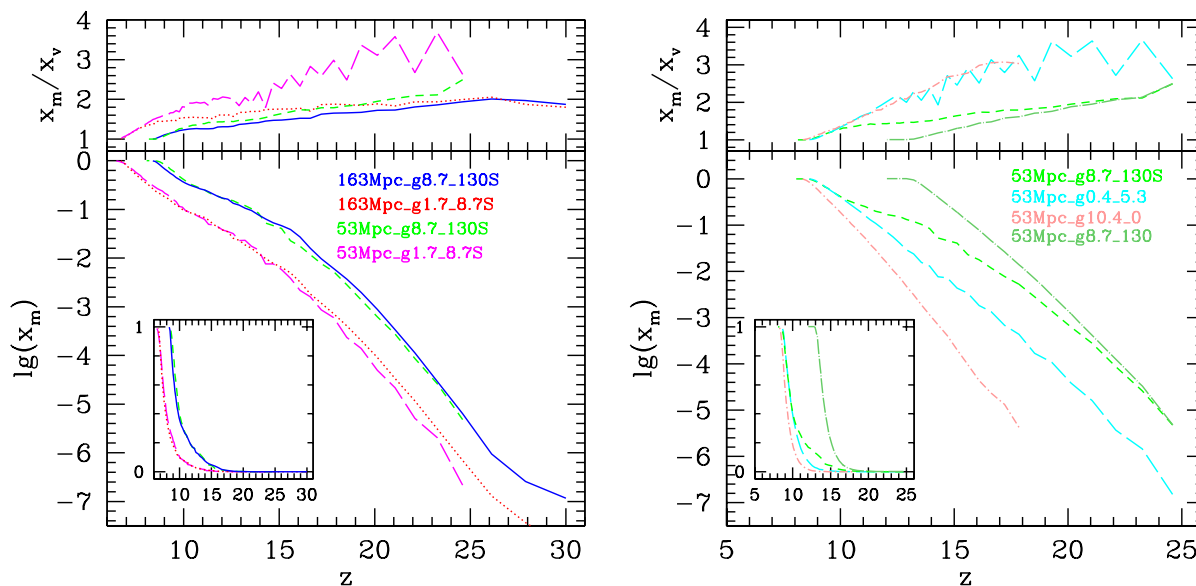


**Figure 9.** (bottom panels) Mass-weighted reionization histories for our fiducial self-regulated cases (left) and with varying assumptions about the ionizing sources and their suppression (right). (top panels) Ratio of the mean mass-weighted and volume ionized fractions,  $x_m/x_v$ . All cases are labelled by color and line-type, as follows: (left) L1 (blue, solid), S1 (green, short-dashed), L2 (magenta, long-dashed), and S2 (red, dotted), (right) S4 (cyan, long dashed), S5 (light red, dot-short dashed), and S3 (light green, dot-long dashed). For ease of comparison we show the fiducial case S1 on both plots.

0.058, which is outside the  $1\text{-}\sigma$  range, but still within  $2\text{-}\sigma$ . On the other hand, the simulation volume (163 vs. 53 Mpc) has little effect on the global reionization histories. This is in agreement with the results in Iliev et al. (2006), which were derived by sub-dividing a  $100 h^{-1}\text{Mpc}$  volume into smaller ones, which indicated that  $\sim 20 - 30 h^{-1}\text{Mpc}$  box is sufficient to reliably derive the global mean reionization history. Most variations between the corresponding large and small box simulations result solely from the different random realizations in the two cases. At early times ( $x_m < 0.01$ ) there are also departures due to cosmic variance - unlike the larger, 163 Mpc, volume the more limited 53 Mpc one does not contain any sources at  $z > 25$  as those are statistically too rare to occur. Even when the very first halos appear in the 53 Mpc volume, they are initially so few that they are subject to very high shot noise fluctuations. Once there are statistically-significant numbers of sources in each size box the reionization histories converge and any fluctuations thereafter are simply due to the different random realizations. There is also some effect from the higher resolution of the small-box simulations, due to the better-resolved density field in those cases, which yields slightly increased recombinations. This effect is rather minor here however, because the relatively small difference in resolution results in only a marginal increase of the recombination rates.

In Fig. 9 (top left panel) we show the ratio of the ionized fraction by mass,  $x_m$  and by volume,  $x_v$ , which is equal to the average density of the ionized regions in units of the mean (Iliev et al. 2006). These ratios start at about 2 and remain above unity at all times, indicating that the reionization proceeds in an inside-out manner, with the high density peaks (where the first sources preferentially form) being ionized on average earlier than the mean and low-density ones. On average the ionized regions are denser in the low-efficiency cases. This behaviour could be expected based on the typically smaller H II region sizes in those cases. They therefore stay in the immediate vicinity of the density peaks and do not

propagate as much into the voids. The higher spatial resolution of the 53 Mpc cases also yields somewhat higher mean density of the ionized regions compared to the corresponding 163 Mpc box cases.

### 4.3 The effects of the source model: photon production efficiencies and minimum source mass

In Fig. 9 (right panels) we show the corresponding reionization history results when the source models are varied. We also replotted one of our fiducial cases, S1, for facilitating direct comparison with the self-regulated cases. All reionization histories remain largely monotonic throughout the evolution, which therefore is a fairly robust feature, independent of the particular ionizing source properties assigned. However, a wide range of overlap epochs - from as early as  $z = 12.9$  in the no suppression case S3 to  $z = 8.3$  in large-source-only case S5, and a wide range of slopes of the reionization history evolution are observed.

Our fiducial case, S1, has the most extended reionization history of all, which starts with the formation of the first  $10^8 M_\odot$  halos at  $z \sim 26$  and reaches overlap at  $z = 8.9$ . In comparison when all sources have the same efficiencies, but none are ever suppressed (case S3) the reionization history is very steep, roughly exponential, tracking the exponential rise of the collapsed fraction in halos (cf. Figure 3). The no-suppression, low-efficiency case S4 also produces a very extended history since it also starts with the formation of the first  $10^8 M_\odot$  halos and, by design, reaches overlap at roughly the same time as S1. However, the sources are necessarily much weaker in that case compared to S1 and S3, and therefore the ionized fraction starts much lower compared to the fiducial simulation and only catches up with the self-regulated case at late times ( $x_m \gtrsim 0.25$ ). Finally, in case S5 only the massive sources are active, and therefore the reionization starts late, at  $z \sim 18$ , but  $x_m$  rises exponentially, in proportion of the collapsed fraction in those massive halos, reaching (again by design) overlap at the

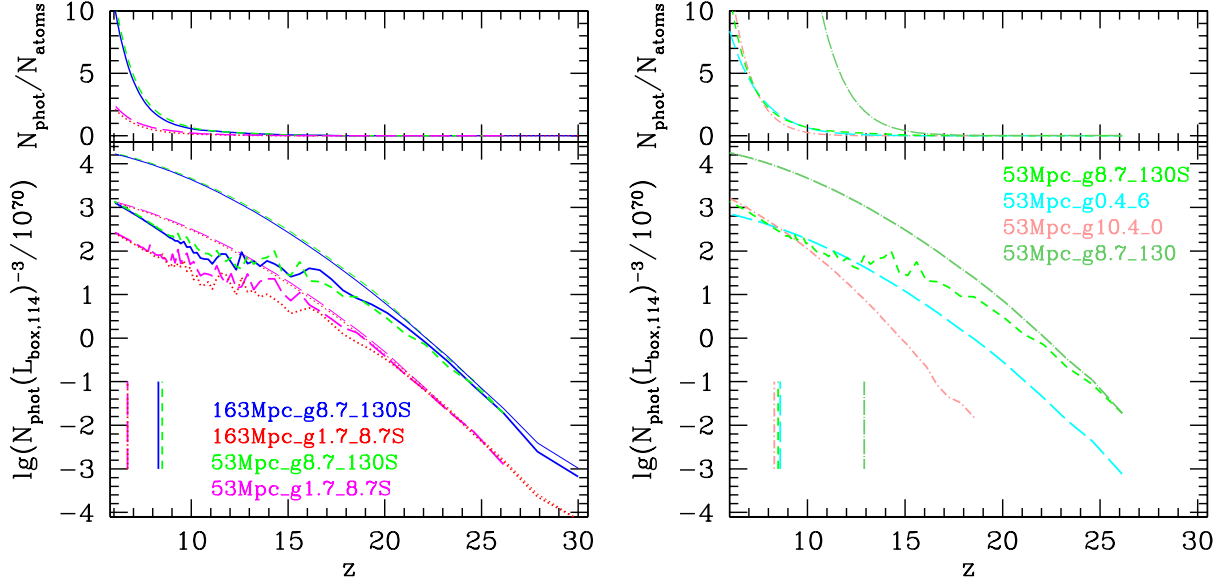


**Figure 10.** (bottom panels) Number of ionizing photons emitted by all sources (i.e. if there were no suppression; thin lines) and all active sources (thick lines) in the computational volume per timestep and (top panels) cumulative number of photons per total gas atom released into the IGM. Notation is the same as in Fig. 9. Vertical lines with same colors and linetypes mark the overlap redshift in each case.

same time,  $z = 8.3$  as the fiducial case. The lack of low-mass halos therefore delays reionization considerably and naturally yields much lower integrated electron scattering optical depth (0.071 compared to 0.084 for S1, and 0.078 for S4).

The mean overdensity of the ionized regions,  $x_m/x_v$  (Fig. 9, top right panel) is above unity for all cases and at all times, demonstrating the robustness of the inside-out nature of reionization, in agreement with our original findings (Iliev et al. 2006). Compared to our fiducial simulation, S1, the ratio  $x_m/x_v$  is significantly higher for cases S4 and S5. This is due to the fact that the H II regions are more tightly correlated with the density peaks in those cases, because the number of sources, which form at the density peaks, rises exponentially in these cases. Finally, simulation S3 show an intermediate behaviour, similar to the fiducial case, S1, but with somewhat faster decrease of the mean overdensity of the ionized regions, due to higher ionization of the low-density regions in this case.

The corresponding evolution curves of the cumulative number of ionizing photons emitted within each simulation are shown in Fig. 10. Indicated are also the number of photons which would have been emitted if no self-regulation has taken place (thin lines) and the overlap redshifts (vertical marks). Starting with our self-regulated cases (Fig. 10, left) we see that the low-mass source suppression does not have a significant impact until  $z \sim 20 - 22$ , but after that has a great impact, reducing the overall number of emitted photons by up to a factor of  $\sim 30$  for highly-efficient low-mass sources and about a factor of 10 for less efficient ones. The number of ionizing photons emitted per timestep also becomes variable and non-monotonic function of redshift due to the complex interplay of suppression and new source formation during the self-regulation process. Eventually, by overlap (indicated for each case by the vertical lines) all low-mass sources are suppressed and the number of photons continues to rise smoothly as ever more high-mass sources form. The simulation boxsize makes little difference in the ionizing photon production, apart from modest variations due to the dif-

ferent random realization in each case. In terms of the cumulative numbers of emitted photons per atom (top panel), by redshift  $z = 6$  up to 10 photons per atom are produced in the efficient-sources case and up to 2 photons per atom in the low-efficiency cases. However, at their respective overlap redshifts approximately the same number are produced, about 1.5, i.e. on average only about one recombination per every 2 atoms occurs during the evolution. Therefore, recombinations are relatively unimportant in these runs. The reason for this is that much of the density fluctuations are at very small scales, well below our radiative transfer grid resolution. This additional small-scale power can be added as sub-grid clumping of the gas, calculated based on much higher resolution simulations. We will consider the effects of sub-grid clumping in a companion paper (Koda et al., in prep.).

Turning our attention to the set of cases with different source efficiency models (Figure 10, right), we first note that the three models which by construction have very similar overlap epochs (our fiducial case, S1, and cases S4 and S5) also have almost identical photon production numbers at overlap. All three reach this point in a very different manner, however. In run S4 all sources are quite weak, but no sources are ever suppressed, and the emissivity per timestep reaches the fiducial case once most low-mass sources are suppressed in the latter case. In case S5 only the massive sources are present and consequently its emissivity lags significantly at early times until eventually the exponential rise of those sources allows it to join the other two cases at  $z \lesssim 11$ . We also note that after overlap the photon emissivity in the no-suppression case S4 lags behind the others because its high-mass sources are very inefficient and the collapsed fraction in low-mass sources by this point does not rise as fast as the one for the high-mass sources. Finally, the number of photons produced in the no suppression, high source efficiency case, S3, simply follows the total collapsed fraction in all sources and therefore rises almost exponentially, roughly parallel to the curve for S4, eventually surpassing 10 photons per atom before  $z = 10$ . However, at its own (very early) overlap epoch



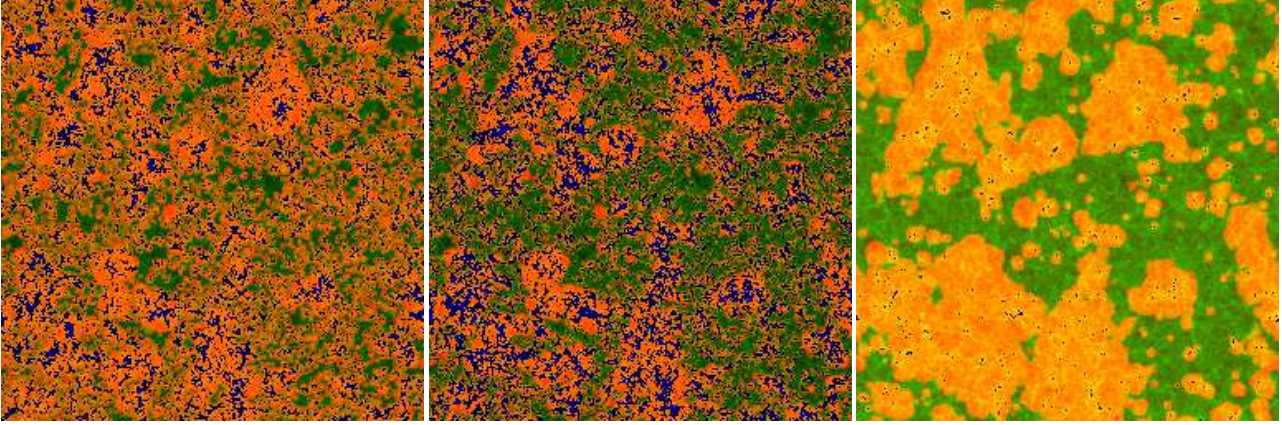


**Figure 11.** Spatial slices of the ionized and neutral gas density from our radiative transfer simulations with boxsize 163 Mpc: (a)(left) L1 (b)(middle) L2, and (c)(right) L3, all at box-averaged ionized fraction by mass of  $x_m \sim 0.50$ . Shown are the density field (green) overlayed with the ionized fraction (red/orange/yellow) and the cells containing active sources (dark/blue).

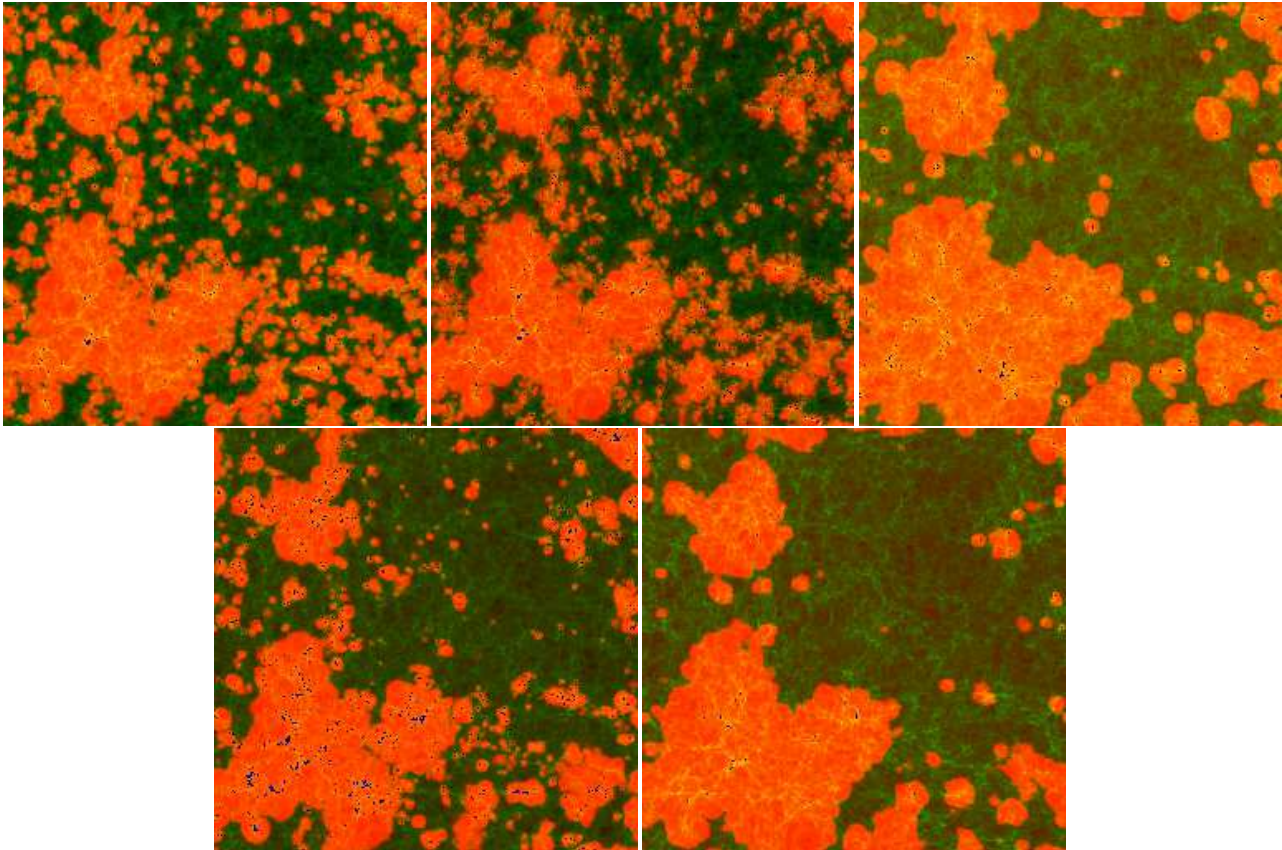


**Figure 12.** Spatial slices of the ionized and neutral gas density from our radiative transfer simulations with boxsize 53 Mpc, all at box-averaged ionized fraction by mass  $x_m \sim 0.50$ . Shown are the density field (green) overlayed with the ionized fraction (red/orange/yellow) and the cells containing sources (dark/blue). Shown are (left to right and top to bottom) cases S1, S2, S3, S4, and S5.

even this case produces the same number of photons as the others, about two per IGM atom.

In Figures 11 and 12 we show slices through our simulation volume showing the geometry of the H II regions at  $x_m \sim 0.5$ , overlayed on the corresponding density field for all our simulations. We also mark the cells containing active sources (blue/dark). Comparing first the large, 163 box cases (Fig. 11), we note that, as could be expected in the high-efficiency fiducial case L1 there are

many more active sources in the low-efficiency one, L2. In contrast, in simulation L3 there are many fewer sources due to its higher mass cutoff, which only leaves the high-mass, rare sources present. The large-scale structures are quite similar in size and shape in the two self-regulated simulations, but the fiducial case L1 yields much more small-scale ionized patches even though it reaches half-ionized state noticeably earlier, at which point there are many fewer, and more clustered, sources. The reason for this apparently

counter-intuitive behaviour is that the much weaker sources in case L2 have difficulties fully ionizing their own cells (which, at 445 kpc/h linear size, are relatively large), and therefore large number of sources are needed to produce a sizeable fully-ionized patch. In contrast, the much more efficient sources in our fiducial case L1 easily ionize their own cell, resulting in many small-size H II regions, instead of the more scattered, partially-ionized cells in L2. On the other hand, in the non-self-regulated case L3 we find many fewer, larger ionized regions, in agreement with our previous results in (Iliev et al. 2008a). The large-scale structures have some similarities to the ones found in the self-regulated cases, as could be expected given that all simulations share the underlying large-scale cosmic structures. However, the ionized regions are in a more advanced stage where they start merging together, and there is far less small-scale structure due to the absence of low-mass, weaker sources. In that case there are also no partially-ionized regions, since there is no low-mass source suppression Jeans-mass filtering (i.e. sources do not die), and all sources are sufficiently luminous to completely ionize their own local volume.

The corresponding images from our small-box simulations at the same ionized fraction of  $x_m \sim 0.5$ , are shown in Fig. 12. Once again, the large-scale structures, which tend to strongly correlate with the underlying distribution of density and clustered halos, are generally quite similar. In contrast, ionized patches produced by multiple, less biased sources whose distribution does follow the knots and filaments of the Cosmic Web are much more irregularly-shaped. There are significant differences in the smaller-scale structures among the range of simulations. The self-regulated cases, S1, S2 and to a lesser extent case S4 have the most small-scale structure, including both small H II regions and rough, irregularly-shaped large H II region boundaries. In contrast, S5, which does not include the low-mass sources and S3, which includes efficient, unsuppressible low-mass sources both yield many fewer ionized patches with smoother boundaries, which reflects the rarity and highly clustered nature of their active sources. We have presented a more detailed discussion of the H II region geometry, size distribution and topological characteristics in a recent companion paper based on a subset of the current suite of simulations (Friedrich et al. 2011).

## 5 OBSERVATIONAL SIGNATURES

We now turn our attention to the reionization observables and specifically how are they related to the assumed source populations and their efficiencies. A better understanding of these dependencies should allow us in turn to use the observational data to constrain the properties of the reionization sources. Our main focus will be on the redshifted 21-cm signatures, although we also briefly discuss the photoionization rates in the IGM, related to the measurements of the Gunn-Peterson effect and the gas temperature.

### 5.1 Photoionization rates

An important, if indirect, observable signature of reionization is the mean photoionization rate in the IGM. At present this quantity has only been measured for the post-reionization IGM at  $z < 6$ , derived based on the small residual neutral fraction and its corresponding Ly- $\alpha$  optical depth. It therefore typically characterizes only the final EoR stages, around and after overlap.

The redshift evolution of the mean photoionization rates,  $\Gamma$ , averaged over our simulation volume for our large-box simulations

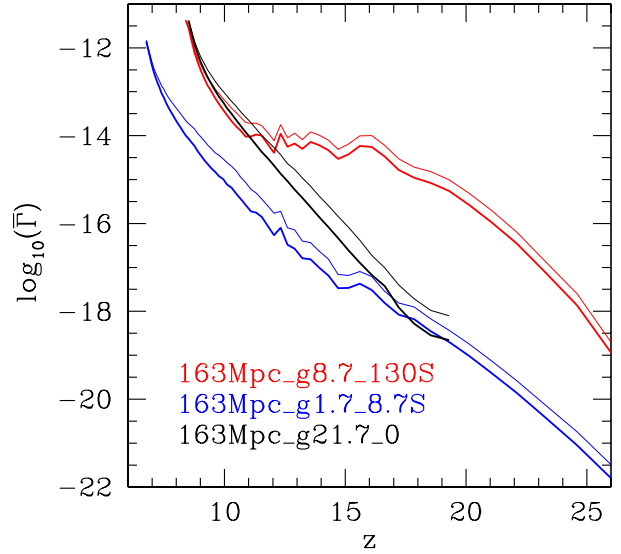


**Figure 13.** Evolution of the mean mass-weighted (thin lines) and volume-weighted (thick lines) photoionization rates in our computational volume for simulations L1 (red), L2 (blue) and L3 (black).

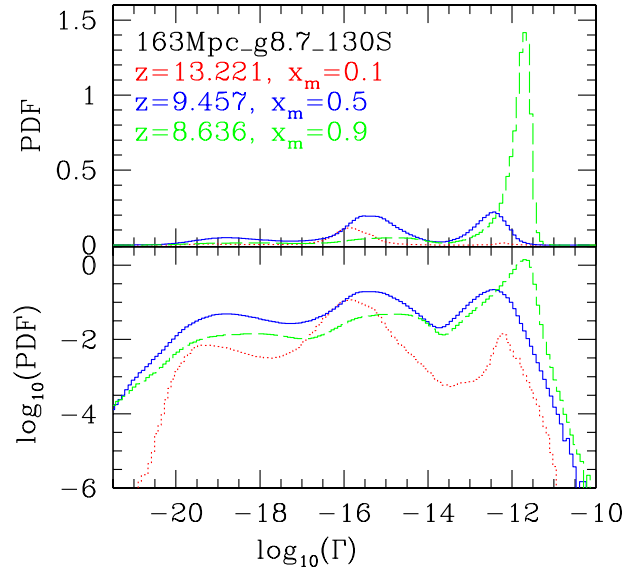


**Figure 14.** Photoionization rate PDF's for our fiducial case L1 for epochs when the ionized fraction by mass is  $x_m = 0.1$  (red),  $x_m = 0.5$  (blue),  $x_m = 0.9$  (green) plotted in linear (top) and log (bottom) scales.

L1-L3 are shown in Figure 13. In overall curve shape and timing the evolution roughly mirrors the reionization histories for these three cases. This is natural, since the mean photoionization rate is average of the fraction from the ionized regions, where the  $\Gamma$  values are high and fairly uniform at  $\sim 10^{-12} \text{ s}^{-1}$  (see also Fig. 14), and the neutral regions, where  $\Gamma \sim 0$ . The mean photoionization rate in our fiducial case L1 initially rise roughly exponentially, until self-



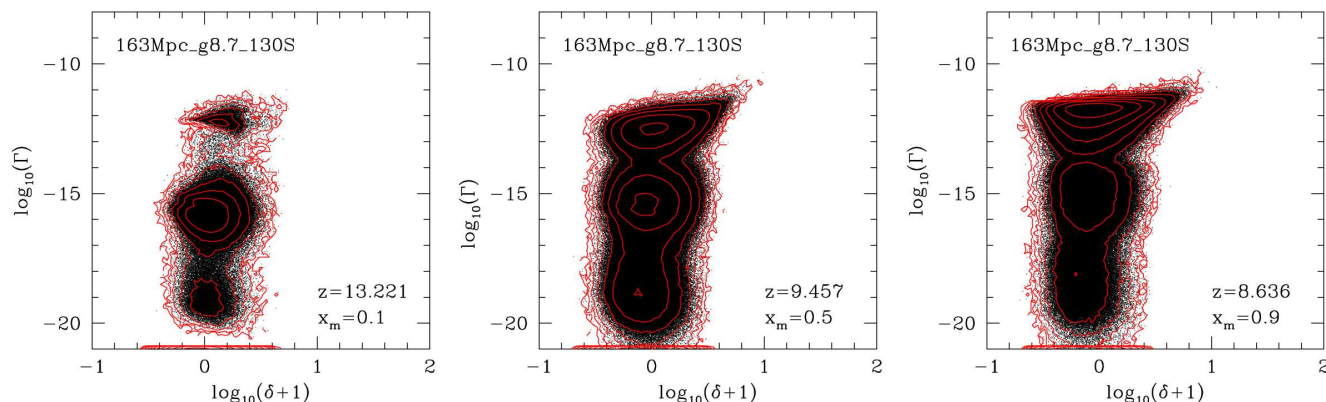


**Figure 15.** Cell-by-cell photoionization rate - overdensity correlation scatter plot at  $x_m = 0.1$  (left),  $x_m = 0.5$  (middle), and  $x_m = 0.9$  (right). Contours are logarithmic, from 10 cells up every 0.5 dex.

regulation becomes wide-spread at  $\sim 16$ , at which point the stall at around  $10^{-14}$  until the high-mass sources become sufficiently abundant to dominate the evolution, which occurs around  $z \sim 11$ . At this time the mean rates resume their steep rise, reaching a peak of  $\Gamma \sim \text{few} \times 10^{-12}$  by overlap. The situation is somewhat different for the low photon production efficiency case, L2. The mean  $\Gamma$  values are much lower in this case, by 2-4 order of magnitude, and are mostly rising monotonically throughout the evolution, as the Jeans-mass suppression effects are milder in this scenario. The peak value reached in this case is about  $10^{-12}$ , in rough agreement with the measured one at  $z \sim 6$ . However, we should note that any direct comparisons to observationally-derived values are at best approximate since our simulations at present do not take into account the Lyman-limit systems (LLS), which are likely to limit the growth of the mean free path of the photons and thus limit  $\Gamma$ , as well. Before overlap the mean free path is dictated by the remaining neutral regions and the (still fairly high) residual neutral gas fraction within the ionized regions, and therefore the LLS are unimportant and do not affect our simulation results. The same is probably not true after overlap and we will study the effects of LLS in future work. For our current purposes the lack of LLS means that we cannot yet make a firm conclusion that the low efficiency, late-overlap case, L2, fits the observations better than case L1.

The mean photoionization rate for the non-self-regulated case L3 is intermediate between L1 and L2. It starts from very low values,  $\sim 10^{-19}$ , when there are still only a very few high-mass sources, around  $z \sim 17$ , but then rise sharply, roughly exponentially, and converges (by construction, since efficiencies were picked so they overlap at the same time) to the values for L1 at later times.

The mass-weighted photoionization rates (thin lines) are significantly higher, by factors of up to 2-3 than the volume-weighted ones (thick lines) at all times and for all simulations. This is easy to understand given the inside-out nature of reionization, whereby the ionizing sources are found in dense regions, which pushes the mass-weighted means higher. Such large differences are interesting, however, since they can possibly skew the observationally-derived values. Probes of the mean, low-density IGM will therefore yield considerably lower values for  $\Gamma$  than any measurements which are more sensitive to denser regions, e.g. around sources.

Several illustrative PDF's (at cell size, here 445 kpc/h) of the

photoionization rates for our fiducial simulation L1 are shown in Figure 14. Plotted are the PDF's at early ( $x_m = 0.1$ ), intermediate ( $x_m = 0.5$ ) and late ( $x_m = 0.9$ ) stages of the evolution. These can be compared to the no low-mass sources data we presented previously in (Iliev et al. 2008b). At all times the PDFs show a characteristic, three-peaked profile. The rightmost peak, at  $\Gamma_{-12} \sim 1$ , is formed by the cells inside the H II regions, while the other two peaks correspond to partially-ionized cells, predominantly at the expanding I-fronts and relic (i.e. recombining) H II regions. As we have shown in (Iliev et al. 2008b), the ionization state is close to or at equilibrium deep inside the ionized regions, but far from equilibrium at the I-fronts. This holds true for the current simulations, as well. However, compared to our previous simulations the low-mass source suppression in the current runs yields a significant fraction of volume in relic H II regions and partially-ionized cells and thus higher peaks at lower  $\Gamma$  values than was observed in the simulations without suppression.

In Figure 15 we show scatter plots and the corresponding contour levels of the local photoionization rates,  $\Gamma$  vs. density in units of the mean,  $1 + \delta \equiv \rho_{\text{cell}}/\bar{\rho}$  for our fiducial case, L1 and  $x_m = 0.1, 0.5$  and  $0.9$ . Overall, there is a clear positive correlation between the density and the photoionization rate. This could be expected, given that sources, around which the photorates peak form preferentially in high-density regions. However, the relationship between the two is complex, the correlation is weak and the scatter significant. Similarly to the PDF's discussed above, three peaks are observed. The high- $\Gamma$  peak ( $\Gamma \sim 10^{-12} \text{ s}^{-1}$ ) consists of the ionized cells, which are typically denser than average. The middle peak, at  $\Gamma \sim 10^{-15} \text{ s}^{-1}$ , corresponds to I-fronts and other partially-ionized regions, while the cells with still lower values ( $\Gamma \sim 0$ ) correspond to the still-neutral regions. At early times ( $x_m = 0.1$ ) the majority of cells is either neutral or partially-ionized and the correlation with the local density is very weak. When the process advances ( $x_m = 0.5$ ) a large population of fully-ionized, high- $\Gamma$  cells develops and within the H II regions the photoionization rate is fairly well correlated with the density, albeit still with a large scatter. On the other hand, for the photoionization rates in the partially-ionized regions shows essentially no correlation with the density. At late times ( $x_m = 0.9$ ) these trends become even more pronounced and a quite tight correlation develops for the highest-density regions. The overall behaviour is consistent with



what we previously observed when no source suppression were present (Iliev et al. 2008b), albeit with some minor quantitative differences.

## 5.2 Redshifted 21-cm

The differential brightness temperature of the redshifted 21-cm emission with respect to the CMB is determined by the density of neutral hydrogen,  $\rho_{\text{HI}}$ , and its spin temperature,  $T_{\text{S}}$  and is given by

$$\begin{aligned}\delta T_b &= \frac{T_{\text{S}} - T_{\text{CMB}}}{1+z} (1 - e^{-\tau}) \\ &\approx \frac{T_{\text{S}} - T_{\text{CMB}}}{1+z} \frac{3\lambda_0^3 A_{10} T_* n_{\text{HI}}(z)}{32\pi T_{\text{S}} H(z)} \\ &= 28.5 \text{ mK} \left( \frac{1+z}{10} \right)^{1/2} (1+\delta) \left( \frac{\Omega_b}{0.042} \frac{h}{0.73} \right) \left( \frac{0.24}{\Omega_m} \right)^{1/2}\end{aligned}\quad (3)$$

(Field 1959), where  $z$  is the redshift,  $T_{\text{CMB}}$  is the temperature of the CMB radiation at that redshift,  $\tau$  is the corresponding 21-cm optical depth, assumed to be small when writing equation 3,  $\lambda_0 = 21.16$  cm is the rest-frame wavelength of the line,  $A_{10} = 2.85 \times 10^{-15} \text{ s}^{-1}$  is the Einstein A-coefficient,  $T_* = 0.068$  K corresponds to the energy difference between the two levels,  $1+\delta = n_{\text{HI}}/\langle n_{\text{H}} \rangle$  is the mean number density of neutral hydrogen in units of the mean number density of hydrogen at redshift  $z$ ,

$$\begin{aligned}\langle n_{\text{H}} \rangle(z) &= \frac{\Omega_b \rho_{\text{crit},0}}{\mu_{\text{H}} m_p} (1+z)^3 \\ &= 1.909 \times 10^{-7} \text{ cm}^{-3} \left( \frac{\Omega_b}{0.042} \right) (1+z)^3,\end{aligned}\quad (4)$$

with  $\mu_{\text{H}} = 1.32$  the corresponding mean molecular weight (assuming 24% He abundance), and  $H(z)$  is the redshift-dependent Hubble constant,

$$\begin{aligned}H(z) &= H_0 [\Omega_m (1+z)^3 + \Omega_k (1+z)^2 + \Omega_\Lambda]^{1/2} \\ &= H_0 E(z) \approx H_0 \Omega_m^{1/2} (1+z)^{3/2},\end{aligned}\quad (5)$$

where  $H_0$  is its value at present, and the last approximation is valid for  $z \gg 1$ . Throughout this work we assume that  $T_{\text{S}} \gg T_{\text{CMB}}$  i.e. that all of the neutral IGM gas is Ly- $\alpha$ -pumped by the background of UV below 13.6 eV from early sources and heated well above the CMB temperature (due to e.g. a small amount of X-ray heating), and thus the 21-cm line is seen in emission. These assumptions are generally well-justified, except possibly at the earliest times (see e.g. Furlanetto et al. 2006b, and references therein).

### 5.2.1 Evolution of the patchiness

In Figure 16 we show space-redshift (space-frequency) slices cut through the simulated image cube as a radio array would see it (ignoring foregrounds). The spatial dimension is on the vertical, where we have duplicated the computational volume for visualization purposes, while the redshift/frequency is along the horizontal. Images are of the 21-cm emission differential brightness temperature signal extracted from our fiducial simulation L1, continuously-interpolated in redshift/frequency including redshift-space distortions due to peculiar velocities. The volume is cut at an oblique angle in order to minimize artificial repetition of structures along any line of sight. The top and middle panel show images (in log, which shows better the residual H I fraction in the ionized regions and linear scale, which shows better the neutral structures) at the full simulation resolution, which is much higher than what current

experiments will achieve given the sensitivity constraints. The bottom panel shows same data, but smoothed with a Gaussian beam and an integrated bandwidth which both roughly correspond to the values adopted in the LOFAR EoR experiment. To mimic the fact that an interferometer such as LOFAR is insensitive to the global signal, the mean signal at every frequency slice has been subtracted.

At high redshift, here  $z > 11$  all H II regions are small and largely isolated. Smoothing the data to the LOFAR resolution (the ones for MWA and GMRT are even lower) renders such small structures undetectable. One needs at least  $\sim 1'$  or better resolution for potentially observing them, making this regime a potential target for future, more sensitive experiments e.g. SKA. However, at intermediate redshifts (here  $z \sim 10$ ) the ionized regions quickly grow by merging and remain clearly visible also after beam- and bandwidth smoothing. Even though some detail is lost, the large-scale structure of the ionization field remains visible all the way to the overlap epoch, here  $z = 8.4$ . As was noted above, compared to the simulations with no self-regulation (e.g. Iliev et al. 2008b), the suppression of low-mass sources introduces much more small-scale structure and many, mostly small partially-ionized and relic H II regions. However, the smoothing to the radio array resolution largely eliminates this fine-scale structure and the result is, at least visually, not dramatically different from the case with no self-regulation. The minimum and maximum values of the differential temperature are also similar. We consider more quantitative measures of the 21-cm signal next.

### 5.2.2 21-cm background: mean and rms

The evolution of the mean differential brightness temperature and its rms fluctuations for our fiducial case L1 and L3, which corresponds to our previous simulations with no self-regulation in (Iliev et al. 2008b) are shown in Figure 17. The presence of low-mass sources and Jeans mass filtering yields initially a steeper decline of the mean 21-cm emission starting from  $\nu \sim 80$  MHz ( $z \sim 17$ ), at which point the low-mass sources start forming in larger numbers (becoming  $\nu \sim 3$  halos, cf. Figure 3), while the high-mass sources are still very rare. At  $\nu \sim 130$  MHz ( $z \sim 10$ ) the high-mass sources in turn become  $3 - \sigma$  halos, i.e. relatively more common and the mean  $\delta T_b$  evolution for case L3 steepens, eventually reaching the same overlap epoch (by construction). In terms of detectability in experiments looking for rapid changes in the 21cm signal as the Universe reionizes (Shaver et al. 1999; Bowman & Rogers 2010), this behaviour means that the case of self-regulation is even more difficult to detect than the one without. While without self-regulation the global signal drops fast by about 25 mK between 130 and 150 MHz, with it the drop at the higher frequencies is more gradual. The decrease with self-regulation is somewhat steeper at lower frequencies,  $\nu = 80 - 120$  MHz, but it is still fairly gradual and more difficult to detect.

Comparing the rms fluctuations averaged over LOFAR-like beam and bandwidth (Figure 17, right) we see that the overall evolution follows similar paths in both cases. Early-on very little of the gas is ionized and the fluctuations therefore simply follow the density ones. Only when a significant ionized fraction develops do the fluctuations depart from the underlying density. For simulation L3 this occurs fairly late, at  $\nu > 110$  MHz, compared to much earlier,  $\nu > 80$  MHz, for the fiducial simulation. At this point the rms fluctuations slightly dip, as the highest density peaks are ionized, which diminishes the mean  $\delta T_b$  but does not boost the fluctuations since the H II regions are still smaller than the smoothing size. As the H II regions grow, the fluctuations increase again, reaching a peak be-

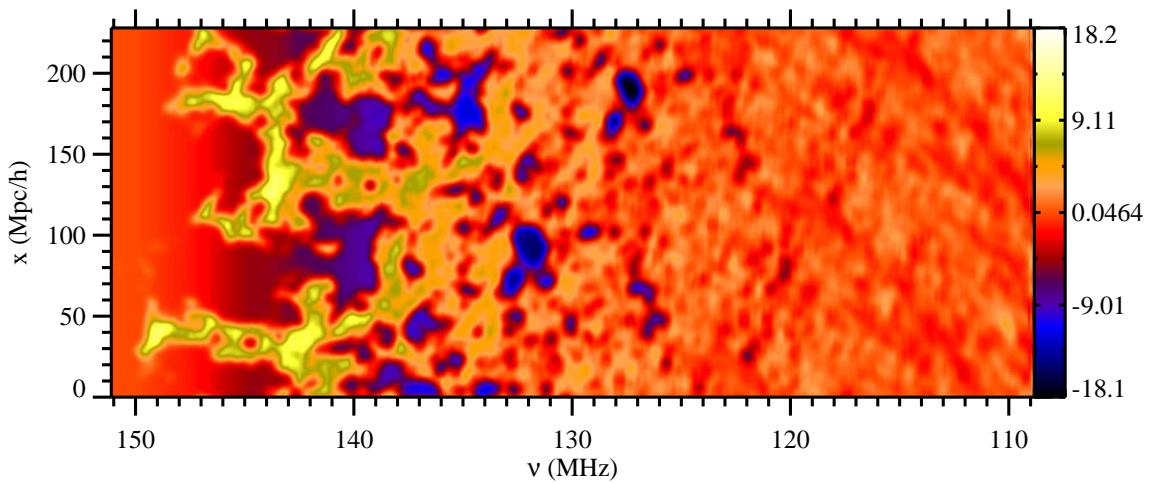
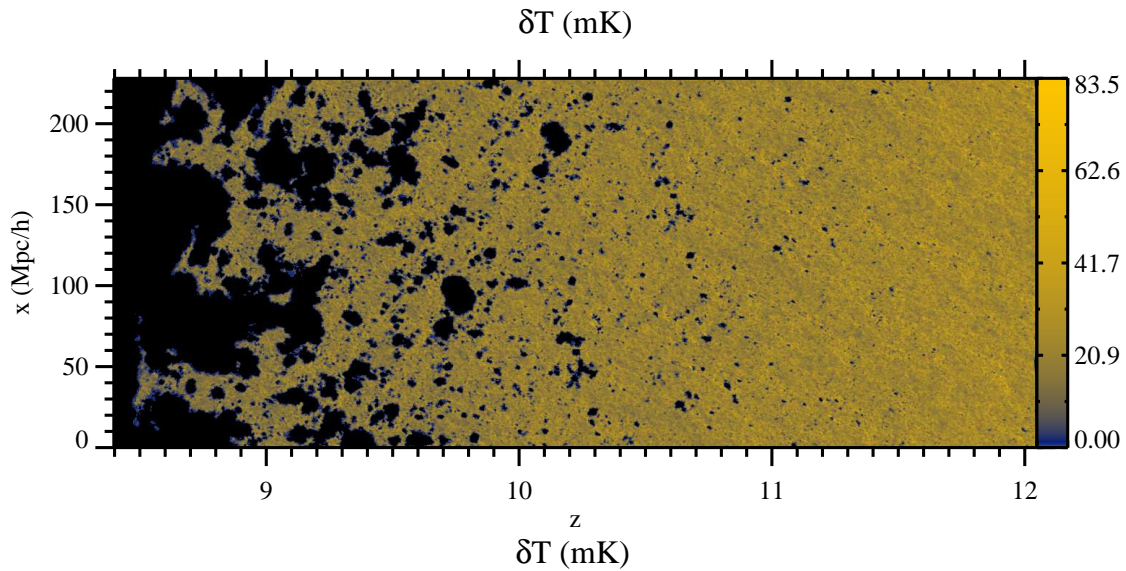
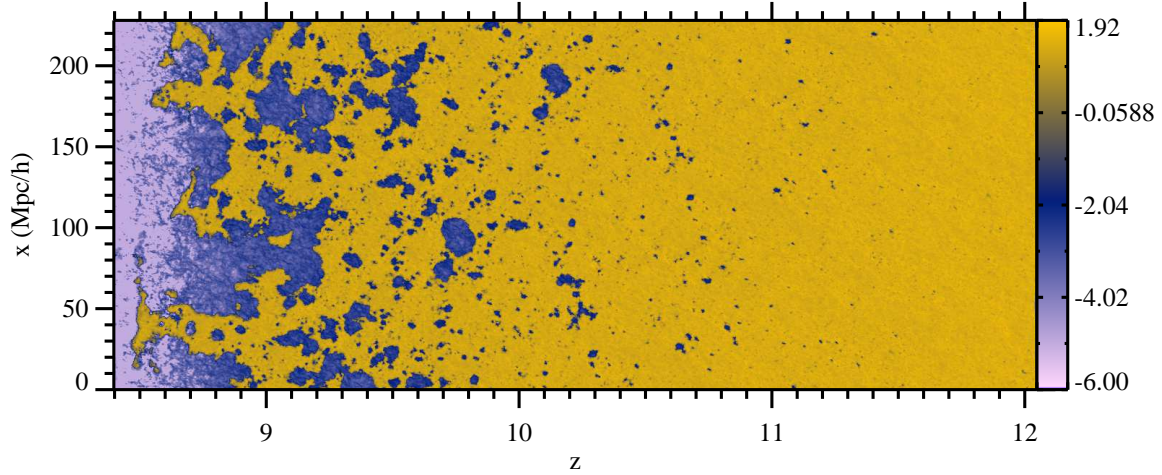


**Figure 16.** Position-redshift and position-frequency slices from our fiducial simulation L1. These slices illustrate the large-scale geometry of reionization and the significant local variations in reionization history as seen at redshifted 21-cm line. Observationally they correspond to slices through an image-frequency volume of a radio array. The top and middle images shows the differential brightness temperature at the full grid resolution in decimal log and linear scale, respectively. The bottom image shows the same  $\delta T_b$  data, but smoothed with a Gaussian beam of  $3'$  and (tophat) bandwidth of 0.45 MHz, roughly corresponding to the expected parameters for the LOFAR EoR observations. In order to mimic the behaviour of an interferometer the mean signal has been subtracted for every frequency slice. The spatial scale is given in comoving Mpc and we note that for visualization purposes we have doubled (periodically) the box size in the spatial direction. The redshift-space distortions due to the peculiar velocities are also included.

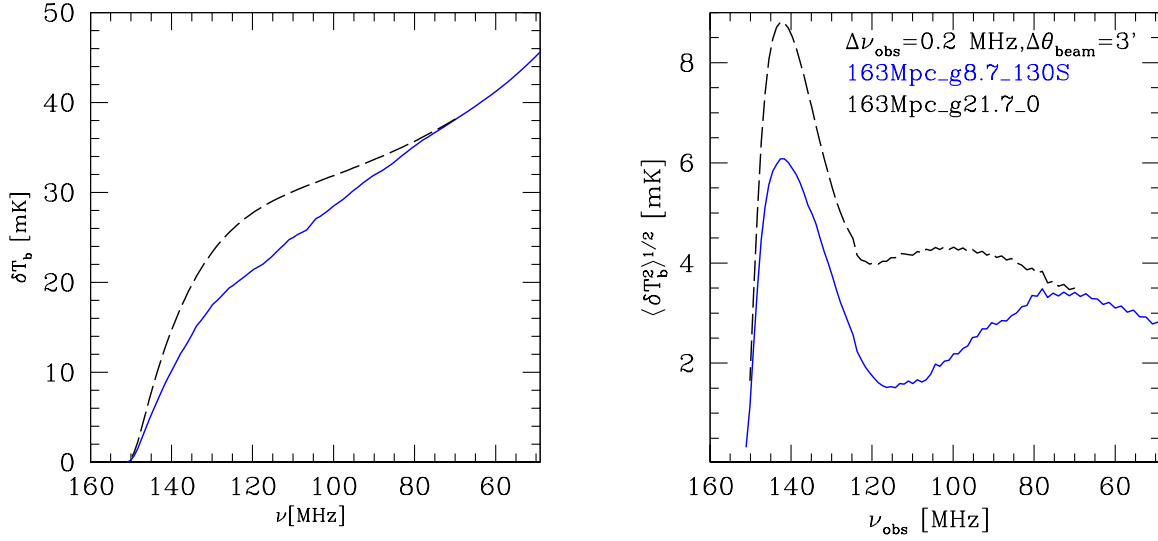


**Figure 17.** The evolution of the mean 21-cm background (left) and its rms fluctuations for Gaussian beams size  $3'$  and bandwidth 0.2 MHz and boxcar frequency filter (right) vs. observed 21-cm frequency. Shown are simulations L1 (blue, solid) and L3 (black, long-dashed).

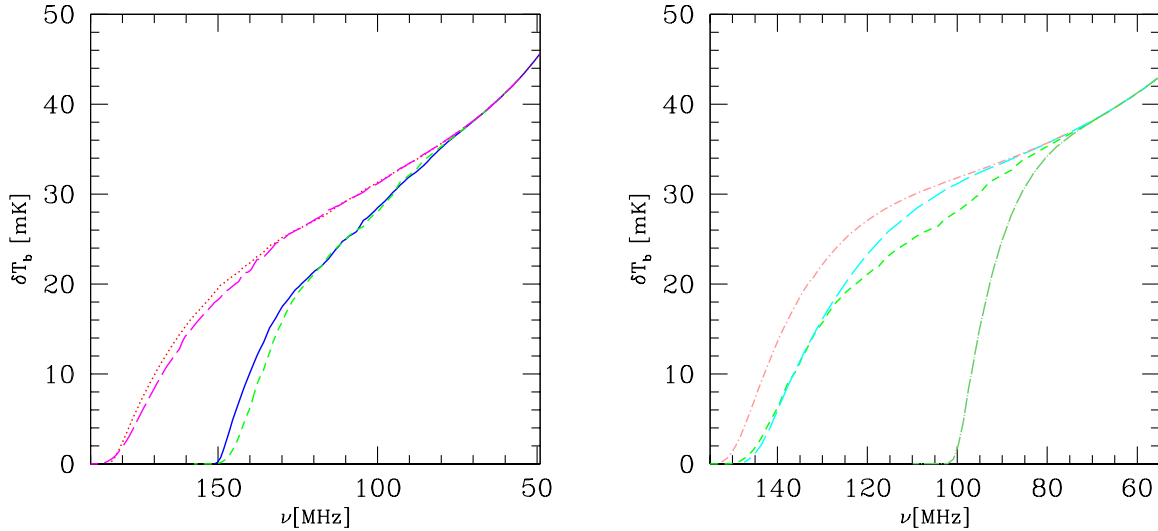


**Figure 18.** The evolution of the mean 21-cm background for our fiducial cases (left) and varying the source model (right). All cases are labelled by color and line-type, as follows: (left) L1 (blue, solid), S1 (green, short-dashed), L2 (magenta, long-dashed), and S2 (red, dotted), (right) S4 (cyan, long dashed), S5 (light red, dot-short dashed), and S3 (light green, dot-long dashed)

fore the signal dips again as the IGM becomes highly ionized. The peak position (at 142 MHz) remains the same in both cases and is thus not affected by self-regulation. The rms fluctuations are lower with self-regulation, by about 1/3 at the peak. The reason for this is the lower mean differential brightness temperature in that case, as can be seen in the bottom panel. When the fluctuations are normalized by the mean they become identical in the two cases once they surpass the density fluctuations ( $\nu > 127$  MHz). Before that point the fluctuations in case L3 closely follow the density ones, while

in case L1 they are lower because the highest-density peaks have already been ionized.

In Figure 18 we show the evolution of the mean redshifted 21-cm differential brightness temperature for high vs. low source efficiencies and different box sizes (left) and for varying source models (right). The lower photon efficiencies (simulation L2) predictably yield a more gradual transition of the global IGM from neutral to ionized state compared to our fiducial case L1. E.g. the evolution from 25 mK to  $\sim 0$  mK occurs over  $\sim 50$  MHz, from 130 to 180 MHz. Such an evolution would make detection of the

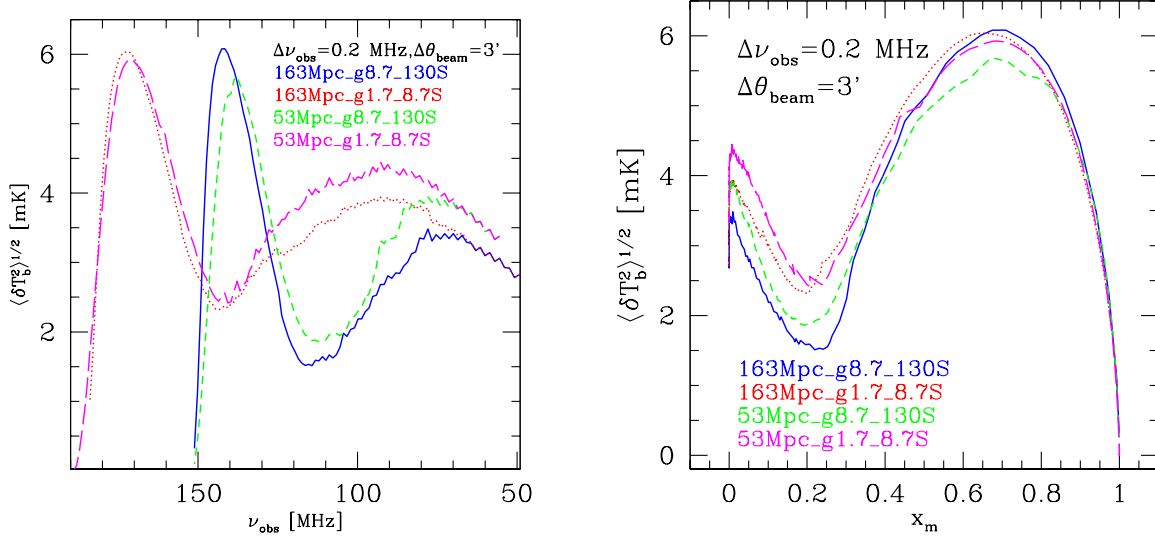


**Figure 19.** The evolution of the rms fluctuations of the 21-cm background, for beamsize  $3'$  and bandwidth  $0.2$  MHz and boxcar filter vs. redshift (left) and vs. mean mass-weighted ionized fraction (right). Shown are our fiducial simulations L1 (blue, solid), S1 (green, short-dashed), L2 (magenta, long-dashed), and S2 (red, dotted).

'global step' even more difficult compared to the fiducial case. The computational volume adopted for the simulation makes very little difference to the predicted mean 21-cm signal, demonstrating again that  $37 \text{ Mpc}/h$  box is sufficiently large to faithfully represent the mean reionization history. Most cases with varying UV-source models (Figure 18, right) yield mean 21-cm histories which are quite similar to each other, a consequence of their analogous reionization histories. The only noticeable differences are at intermediate frequencies, between 90 and 130 MHz, where case S4 gives higher  $\delta T_b$  by up to 5 mK. The only significantly different evolutions are provided by cases S5 and S3. Those scenarios exhibit sharper 21-cm step due to their faster, exponential rise of the ionizing photon emissivity due to the weak or no suppression in those cases.

The evolution of the rms 21-cm emission fluctuations for LOFAR-like beam and bandwidths corresponding to the same sets of simulations as in Figure 18 are shown in Figures 19 (high vs. low ionizing efficiencies and varying boxsize) and 20 (different UV source models). We show the same data vs. observed frequency (left) and ionized fraction (right). The latter takes away the reionization timing and allows comparison at the same stages of each reionization history regardless of when they actually occur in time.

In all cases the rms evolution roughly follows the same path, with an initial rise tracking the underlying density fluctuations when the IGM is mostly neutral, with a subsequent decrease when the first H II regions appear followed by a second, higher peak of the fluctuations at later times when the initially small ionizing regions grow, overlap locally and as a result match better the interferometer beam and bandwidth resolution, and a final decline when most hydrogen is ionized. However, despite this recurring pattern, there are significant, interesting, and often instructive differences among the models. Varying the ionizing photon emission efficiencies primarily changes the timing of the peak of the fluctuations (Figure 19, left), from 142 MHz ( $z = 9$ ) for the fiducial case L1 to 172 MHz ( $z = 7.24$ ) for the low-efficiency case L2. However, as

seen in Figure 19 (right) this shift to later times is fully explained by the delayed reionization in the low-efficiency model and both curves peak at mass-weighted ionized fraction  $x_m \sim 0.7$ . We note that the latter value is dependent, apart from the reionization parameters, also on the beam and bandwidth considered, as the peak is reached when the typical H II region size is best matched to the radio array resolution, therefore the peak occurs earlier in the reionization history for higher resolution and later for lower one. The fluctuation dip due to the earliest H II regions also occurs at the same point of the reionization history ( $x_m \sim 0.2 - 0.25$ ) in both cases, but the lowest rms values reached differ significantly at 1.5 mK for the fiducial model vs. 2.3 mK for the low-efficiency one. The reason for this is that in the former case the bottom occurs earlier, when the sources responsible are rarer, more biased and therefore ionize the highest density peaks, which results in a larger decrease in the fluctuations. The simulation volume (and, correspondingly, radiative transfer grid resolution) has moderate, but appreciable effect on the 21-cm fluctuations in our fiducial case. The peak height is decreased by 7%, from 6.1 mK to 5.7 mK, but it is also shifted to earlier time/lower frequency (to 138 MHz). Interestingly, while the dip of the fluctuations is also shifted to lower frequency for the smaller box simulation, the lowest rms value is in fact higher. At first sight this appears counter-intuitive, since naively we might expect that the higher grid resolution in the smaller volume to yield a larger rms decrease (since the density peaks where the first sources form are resolved better in this case). What actually occurs here is more complicated, however. Statistically, there are fewer (and lower) high-density peaks in the smaller volume, which diminishes the effect of the very first sources on the fluctuations. Furthermore, the very first sources form later in the smaller box, again due to its much smaller volume, which means that the 21-cm rms fluctuations track the density ones for somewhat longer. On the other hand the effects of box size and resolution for the low-efficiency cases are small and manifest themselves solely through the higher underlying density fluctuations in the small-box, high-

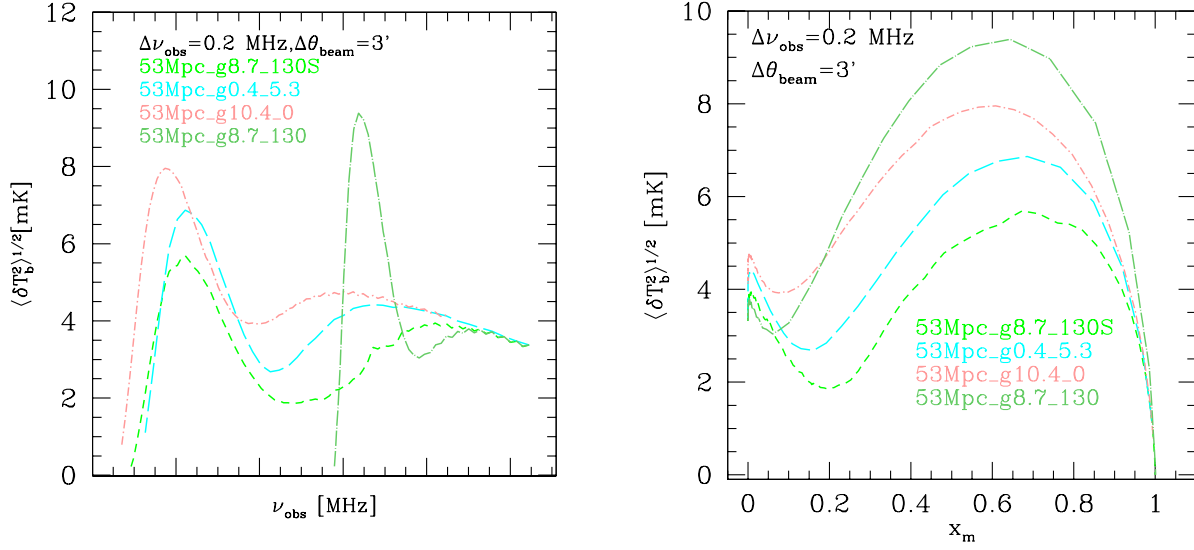


**Figure 20.** Same as Fig. 19, but for varying UV source models: S1 (green, short-dashed), S4 (cyan, long dashed), S5 (light red, dot-short dashed), and S3 (light green, dot-long dashed).

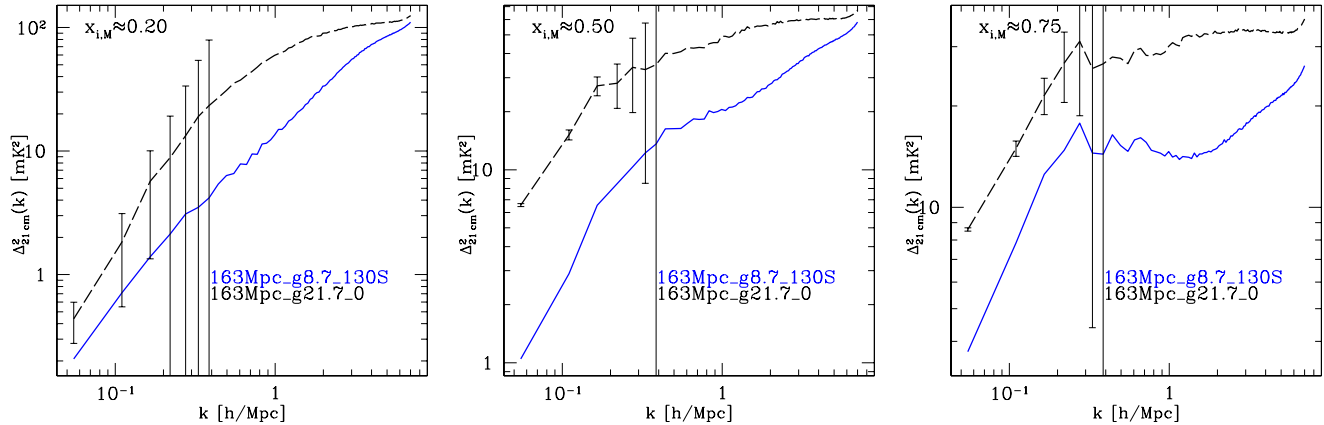


**Figure 21.** The effect of self-regulation on the 21-cm differential brightness temperature fluctuation power spectra. Shown are the epochs at which the ionized fractions are (left)  $x_m = 0.2$ , (middle)  $x_m = 0.5$  and (right)  $x_m = 0.75$  for our fiducial self-regulated case, L1 (blue, solid) and the corresponding non-selfregulated case with same overlap epoch, L3 (black, long-dashed).

resolution simulation. Both the peak and dip reach the same value for the two cases and occur at the same frequencies.

On the other hand, variations of the ionizing source model, yield a wider variety of 21-cm rms evolutions (Figure 20). Interestingly, all models exhibit the basic evolution features seen in our fiducial simulations - the initial dip of the rms value when the first H II regions appear, followed by a (relatively narrower) peak at later times when the process is sufficiently advanced for the typical patch size to roughly match the radio beam and bandwidth (though we note that more extreme, and unrealistic, source models can produce rms fluctuations with a very different shape, see Appendix A). There are significant variations in the details of the evolution, however. The simulations with no low-mass source suppression but same overlap as in our fiducial case (S4 and S5) yield rms fluctuations peaks which are at roughly the same frequency

as the fiducial case ( $\nu \sim 140$  MHz, more specifically), but the  $\langle \delta T_b^2 \rangle^{1/2}$  peak values are up to 50% higher ( $\sim 7 - 8$  mK). The early reionization, no suppression case, S3, gives a still higher peak value, reaching almost 10 mK, and a narrower peak.

A different way to consider the same data is to plot the differential brightness temperature evolution in terms of its own reionization history, i.e. against the mass-weighted ionized fraction,  $x_m$ , (Figure 20, left), which removes the dependence on the absolute timing of reionization. There is only a modest variation in the reionization stage (i.e. ionized fraction,  $x_m$ ) at which the rms peak is reached, which ranges  $x_m \sim 0.6 - 0.7$  (i.e. relatively late in the reionization history). However, as we noted above, the peak value itself varies significantly between the simulations. It is highest for the high-efficiency, no suppression model, S2 ( $\langle \delta T_b^2 \rangle^{1/2} = 9.4$  mK compared to 3.8 mK for our fiducial case S1). Lower efficiency and



no suppression (S4) results in a significantly lower peak (6.9 mK), while when only massive halos are present (L5) the peak is again quite high ( $\langle \delta T_b^2 \rangle^{1/2} = 8.0$  mK). Therefore, in general more abrupt reionization scenarios (S3, S5) result in higher fluctuations at the peak, while more extended ones (due to self-regulation or lower efficiencies) give lower rms peak values.

### 5.2.3 21-cm background fluctuations: power spectra

We now turn our attention to the (3D) power spectra of the 21-cm emission derived from our simulations. We construct the brightness temperature datacube in the redshift space using what we term the *PPM-RRM* scheme, as follows. We first develop an adaptive-kernel, SPH-like approach to compute the bulk-flow velocity of the IGM at any position, directly from N-body particle data. We paint the particle mass by the hydrogenic neutral fraction of the RT grid that the particle resides. Then N-body particles are Doppler-shifted to their apparent locations by LOS bulk-flow velocity, new smoothing kernel lengths are computed using the new particle positions in redshift-space, and halo-excluded particle data (i.e., H I mass) are again smoothed onto a regular, redshift-space grid at RT grid resolution. Then we compute the redshift-space HI density fluctuation, and 21-cm brightness temperature measured in redshift space by

$$\delta T_b^s(\mathbf{s}) = \widehat{\delta T}_b(z_{\text{cos}}) [1 + \delta_{\rho_{\text{HI}}}^s(\mathbf{s})], \quad (6)$$

where  $\widehat{\delta T}_b$  was defined in equation 3. We compute the redshift-space power spectrum using FFT. We refer the reader to Mao et al. (2011) for a detailed discussion of this methodology.

In Figure 21 we compare the 21-cm power spectra for models L3 (equivalent to our previous simulations with no self-regulation) and our fiducial self-regulated case L1 for several representative stages of reionization. In both cases the 21-cm power spectra are initially close to a power law, with no characteristic scale, and with only the L3 power flattening out at small scales due to its lack of very small-scale structures and smooth, large H II regions. Overall, there is always less power in our fiducial case, by factor of 50% (in  $\Delta_k$ ), or more. As ionized regions continue to expand a characteristic scale starts to emerge, which for these particular simulations is around wavenumbers  $k \sim 0.2 - 0.8$  h/Mpc. Interestingly, this feature shows up at the same scales regardless of the presence of low-mass sources, indicating that the characteristic H II region size is caused by the clustering of the high-mass, unsuppressible sources.

On the other hand, the assumed ionizing source efficiencies have at most only a minor effect on the power spectra once the self-regulation is included (Figure 22). The characteristic H II region scale is the same in the two cases and arises at the same point in the reionization history. The modest differences in the power spectra at the early stages of reionization arise due to the preferential ionization of the high density peaks (where the first sources form). At the same ionized fraction  $x_m$  there are many more sources in the low-efficiency case, forming very small H II regions, vs. fewer, larger ones in the high-efficiency case. As a result, the low-efficiency model yields less power at very small scales ( $k > 4$ ), but a little more power at intermediate scales ( $k = 0.2 - 2$ ). At the middle and late stages of reionization the two power spectra at the same  $x_m$  are largely identical, with only small differences due to the different amount of small-scale structure. The simulation volume utilized also has little effect on the derived power spectra at early times, essentially just shifting the range of  $k$  over which the results obtained are reliable. However, as the H II regions grow at intermediate and late stages of reionization, their sizes become comparable

to the simulation volume and as a result the  $37/h$  Mpc volume cannot represent the bubble size distribution correctly and the calculated power spectra completely miss the characteristic H II region scale. On the other hand, the smaller volumes yield more fluctuation power at small scales, due to their superior spatial grid resolution. These results argue for a strong caution when using small (sub-100/h Mpc) boxes for predicting any EoR observables at late times.

Turning our attention to the varying source models (Figure 23), several trends become clear. The lack of Jeans mass filtering (case S3 vs. the fiducial S1) results in much more power at large scales ( $k < 5$  h/Mpc early,  $k < 2$  h/Mpc at late times), but considerably less power on small scales, consequence of the large H II regions with smooth boundaries in case S3 produced by its luminous and strongly clustered sources. This also results in very flat power spectra for S3, with roughly constant power at all scales at intermediate and late times ( $x_m = 0.5$  and  $0.9$ ). On the other hand, if the low-mass sources are not present at all (case S5 vs. S3) there is more power on all scales during the early stages of reionization ( $x_m = 0.1$ ). However, at intermediate and late stages of reionization the power spectra for the large-source only case S5 remain steeper, with considerably more power at small scales, which results in cases S3 and S5 power spectra crossing at  $k \sim 2$  h/Mpc. The reason for this somewhat counterintuitive behaviour is that the same reionization stage is reached in S5 much later than in S3, by which time there are many more and less clustered high-mass sources, which in turn results in more power at small scales. Finally, the low-efficiency case with no self-regulation (S4) yields very similar power spectra to our fiducial simulation S1 throughout the evolution, with only slightly more power at large scales during the early and intermediate stages, and slightly less small-scale power at the late stages. This suggests that the S1 and S4 scenarios might be difficult to distinguish solely through power spectra measurements.

### 5.2.4 21-cm background fluctuations: PDFs and non-Gaussianity

The 21-cm power spectra would fully characterize the emission field if the differential brightness distribution were purely Gaussian. However, generally that is not the case during reionization, as we have shown in previous work (Mellema et al. 2006b; Iliev et al. 2008a; Harker et al. 2009). The probability distribution functions (PDFs) of  $\delta T_b$  could be significantly non-Gaussian, particularly at the later stages of reionization (Mellema et al. 2006b) and their measured skewness can be used to discriminate between different reionization scenarios (Harker et al. 2009). The PDF's and their evolution could also be used to derive the reionization history of the IGM (Ichikawa et al. 2010; Gluscevic & Barkana 2010).

The 21-cm cell-by-cell PDFs with and without the presence of low-mass, suppressible sources at three representative stages of reionization ( $x_m = 0.1, 0.5$  and  $0.9$ ) are shown in Figure 26. Early on ( $x_m = 0.1$ ) the distributions are mostly following the underlying density field, and as a consequence are mostly Gaussian. There is a non-Gaussian tail for high differential brightness temperatures due to density nonlinearities. Reionization itself introduces some non-Gaussianity at low  $\delta T_b$  as the first H II regions form around the highest density peaks, moving the corresponding cells into the extreme left of the distributions (i.e. holes in the neutral gas distribution, with  $\delta T_b \sim 0$ ). This slightly skews the distribution towards below-average (i.e. negative in  $\delta T_b - \overline{\delta T_b}$ ) temperature values since the low-density regions remain more neutral, on average.

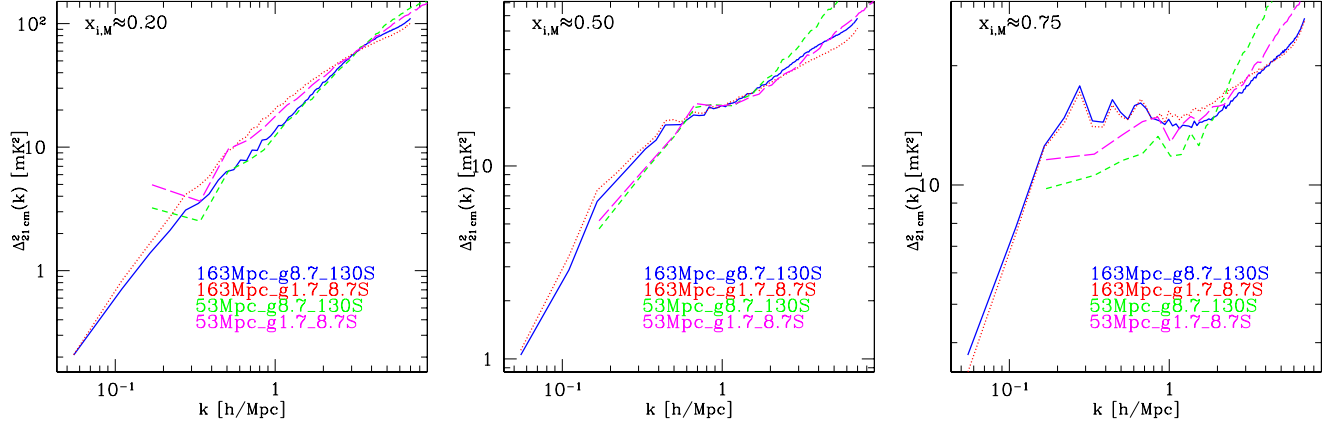


**Figure 22.** 21-cm differential brightness temperature fluctuation power spectra. Shown are the epochs at which the ionized fractions are (left)  $x_m = 0.2$ , (middle)  $x_m = 0.5$  and (right)  $x_m = 0.75$ . All cases are labelled by color and line-type, as follows: L1 (blue, solid), S1 (green, short-dashed), L2 (magenta, long-dashed), and S2 (red, dotted).

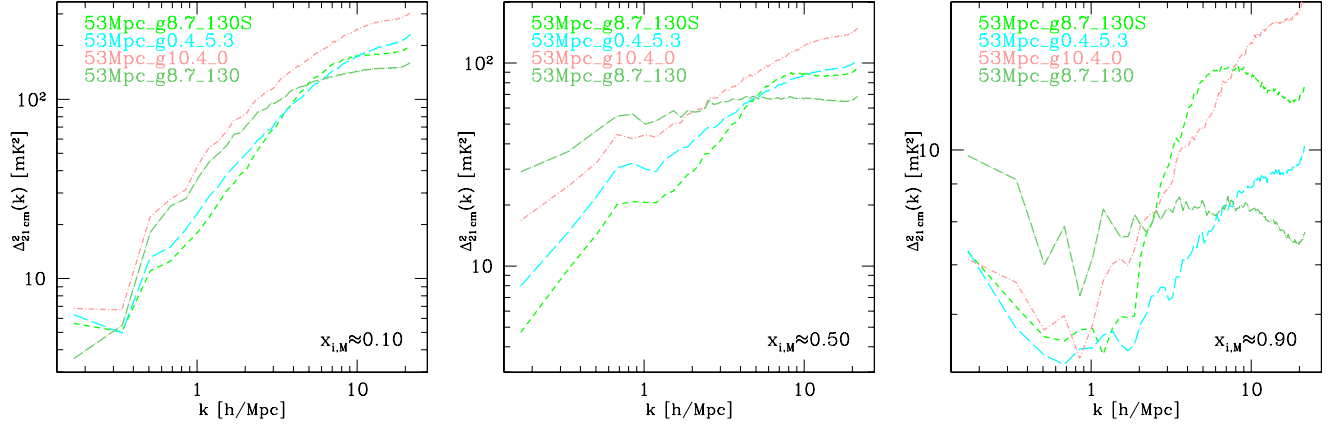


**Figure 23.** 21-cm differential brightness temperature fluctuation power spectra for varying source models. Shown are the epochs at which the ionized fractions are (left)  $x_m = 0.1$ , (middle)  $x_m = 0.5$  and (right)  $x_m = 0.9$ . All cases are labelled by color and line-type, as follows: S1 (green, short-dashed), S4 (cyan, long dashed), S5 (light red, dot-short dashed), and S3 (light green, dot-long dashed)

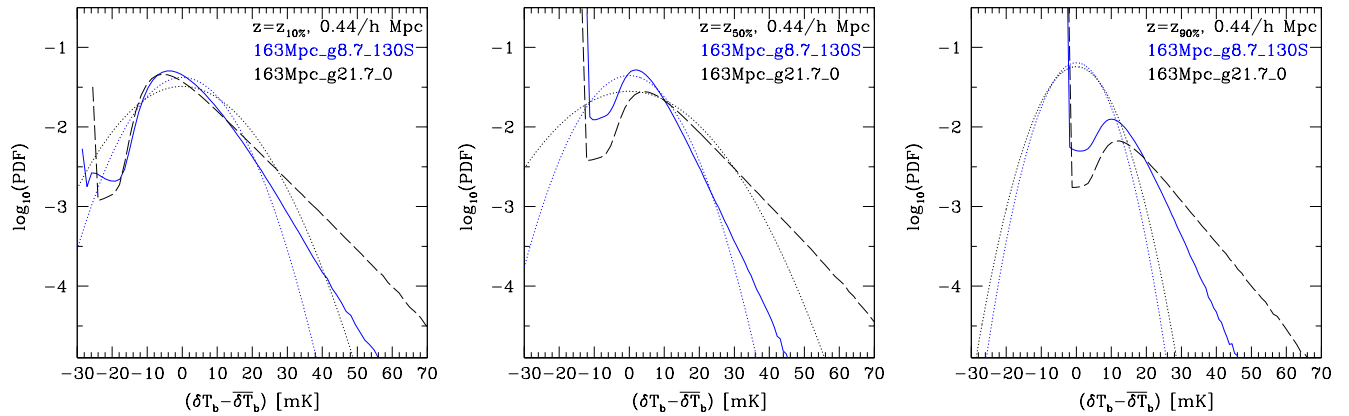


**Figure 24.** The effect of self-regulation on the PDF distribution of the 21-cm signal. Shown are the epochs at which the ionized fractions are  $x_m = 0.1$  (left),  $x_m = 0.5$  (middle) and  $x_m = 0.9$  (right) for our fiducial self-regulated case, L1 (blue, solid) and the corresponding non-selfregulated case with same overlap epoch, L3 (black, long-dashed). The PDFs are cell-by-cell (i.e. no smoothing apart from the numerical grid resolution) Also indicated are the Gaussian distributions with the same mean values and standard deviations (dotted lines, corresponding colours).



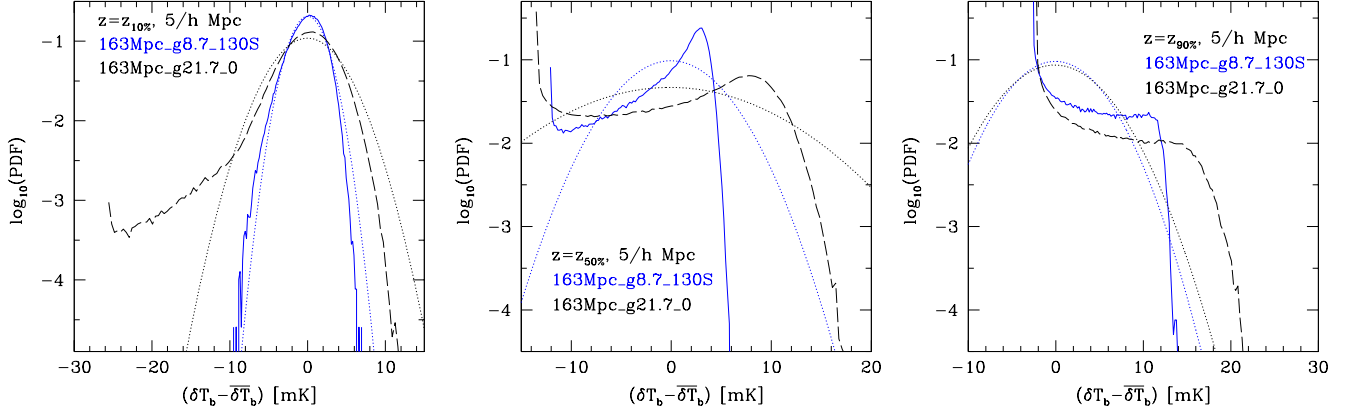


**Figure 25.** Same as in Fig. 24, but for boxcar smoothing of  $5 h^1$  Mpc.

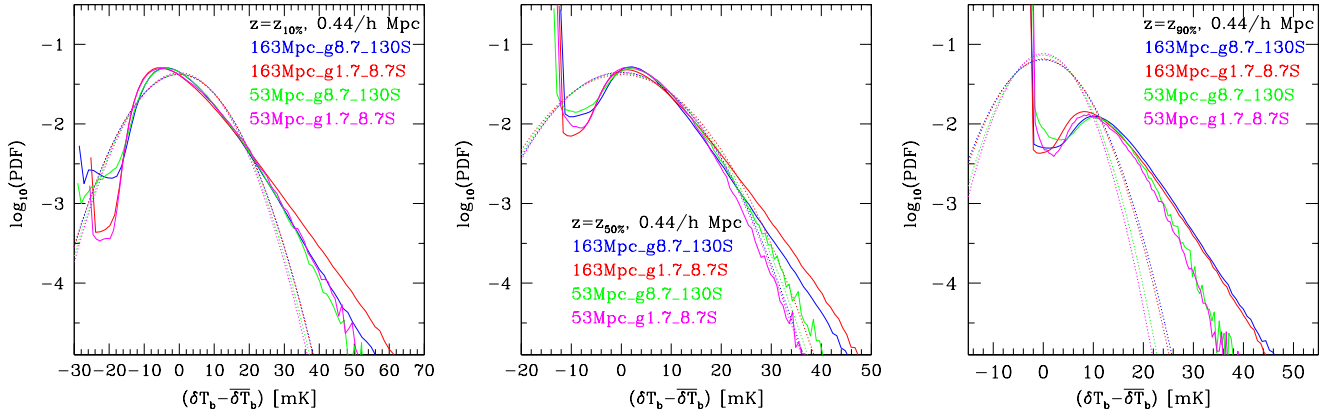


**Figure 26.** The effect of the source efficiencies (high- vs. low efficiency) and box size on the PDF distribution of the 21-cm signal. Shown are the epochs at which the ionized fractions are  $x_m = 0.1$  (left),  $x_m = 0.5$  (middle) and  $x_m = 0.9$  (right) for our fiducial self-regulated cases, L1 (blue, solid), L2 (red, solid), S1 (green, solid), S2 (magenta, solid). The PDFs are cell-by-cell (i.e. no smoothing apart from the numerical grid resolution). Also indicated are the Gaussian distributions with the same mean values and standard deviations (dotted lines, corresponding colours).

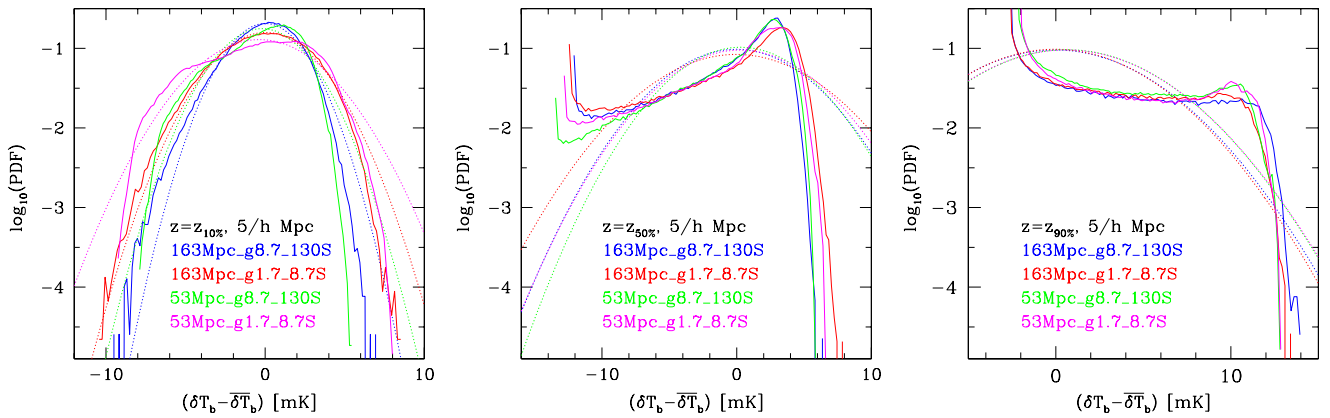


**Figure 27.** Same as in Fig. 26, but for boxcar smoothing of  $5 h^1$  Mpc.

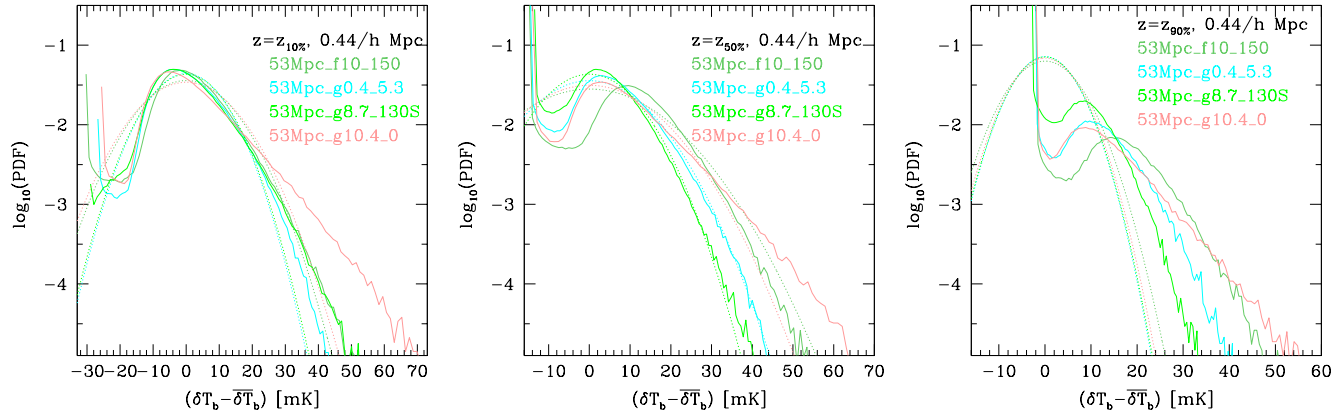


**Figure 28.** The effect of varying source models on the PDF distribution of the 21-cm signal. Shown are the epochs at which the ionized fractions are  $x_m = 0.1$  (left),  $x_m = 0.5$  (middle) and  $x_m = 0.9$  (right) for our fiducial self-regulated case, S1 (green, solid), S4 (cyan, solid), and S5 (light red, solid). The PDFs are cell-by-cell (i.e. no smoothing apart from the numerical grid resolution). Also indicated are the Gaussian distributions with the same mean values and standard deviations (dotted lines, corresponding colours).

Self-regulation mitigates those trends somewhat, as the low-mass sources are less clustered and more uniformly distributed throughout the volume, rather than being only at the highest density peaks (which are strongly clustered, as a consequence of the Gaussian density field statistics, see Figure 6). For the same reasons the PDF with self-regulation is also slightly less wide than without, as evidenced by the Gaussian distributions with the same mean and width as the actual PDFs. During the later stages of reionization the distribution becomes ever more non-Gaussian, with the most prominent feature due to the ionized regions ( $\delta T_b - \bar{\delta T}_b < 0$ ). The remaining neutral regions are a mixture of voids (low, but positive  $\delta T_b - \bar{\delta T}_b$ ) and a few remaining higher-density regions (e.g. filaments) which form the 21-cm bright non-Gaussian tail. Once again, both features are much reduced when low-mass source suppression is taken into account due to the weaker clustering of such sources. The width of the PDFs decreases over time, and does so faster when the low mass sources are not present. At late times the two distributions have almost the same means and widths, although the actual distributions remain significantly different.

When the same PDFs are smoothed with a  $5 \text{ Mpc } h^{-1}$  window (roughly similar in size to e.g. the LOFAR beam, albeit here we use a different window shape for simplicity of the calculations) the results become notably different (Figure 27). The smoothed PDFs at early times ( $x_m = 0.1$ ) become significantly more Gaussian, although some residual non-Gaussian tails remain at both high and low  $\delta T_b$ . As could be expected, the smoothed distributions also become much less wide compared to the unsmoothed ones, since the smoothing window averages the values, flattening the highest peaks and deepest valleys of the distributions.

Interestingly, at the middle and late stages of reionization ( $x_m = 0.5$ , and  $0.9$ ) the opposite happens, namely that the smoothed PDF distributions become less Gaussian for any  $\delta T_b$  value. The PDF distributions with and without self-regulation have similar shapes, but the presence of low-mass sources makes the distribution much less wide. For  $x_m = 0.5$  the very brightest peaks are fewer than a Gaussian would predict, but there are many more intermediate-brightness ( $5 \text{ mK} < \delta T_b - \bar{\delta T}_b < 12 \text{ mK}$  with no self-regulation,  $\delta T_b - \bar{\delta T}_b < 5 \text{ mK}$  with) ones. At the late stages of reionization ( $x_m = 0.9$ ) both cases show many more bright peaks ( $10 \text{ mK} < \delta T_b - \bar{\delta T}_b$ ) than a Gaussian would pre-

dict, although the self-regulated case yields fewer very bright peaks ( $15 \text{ mK} < \delta T_b - \bar{\delta T}_b$ ) than either the corresponding Gaussian or the non-self-regulated case. Finally, regardless of the above differences in the PDFs, their equivalent widths are very similar for the two simulations.

The PDFs for our fiducial self-regulated high- and low-efficiency cases L1, L2, S1 and S2 are shown in Figures 26 and 27. Unlike the presence and self-regulation of low-mass sources presented above, which influenced the PDFs significantly, neither the source efficiencies nor the box size have any dramatic effect of the resulting PDFs. The smaller boxes do not capture well the bright wing of the distribution because the highest density peaks are rare and the volume in these cases is too small to capture them. The effect of varying source efficiency manifests itself by yielding more bright peaks during the early stages of reionization and somewhat brighter peaks at its middle stages.

Finally, the results with a varying source models are shown in Figures 28 and 29. Here for clarity we just show a representative sub-sample of our full simulation suite. Upon inspection several general trends become clear. If only high-mass sources are present (model S5) the distributions are noticeably wider, with a long non-Gaussian tail at high differential brightness temperatures ( $\delta T_b - \bar{\delta T}_b > 30 - 40 \text{ mK}$ ) than in the fiducial self-regulation case, S1. Conversely, there are many fewer regions with low, but positive (i.e. still mostly neutral) differential brightness temperatures ( $\delta T_b - \bar{\delta T}_b < 15 \text{ mK}$ ). The reason for this is that the massive sources form only at the highest density peaks, leaving neutral many other density peaks which have not yet collapsed. The high-density, neutral gas in those peaks is reflected in the non-Gaussian tail at high differential brightness temperatures. Lastly, model S4 (low efficiency sources and no suppression) yields intermediate PDF between the fiducial run and the high-mass sources only runs. The PDF's are therefore mostly dependent on which population of sources is active (high or low mass), but are not very sensitive to the details of the reionization history (models S5 and S8, not shown here, which have the same source population active, but with different efficiencies over time and thus different reionization history yield very similar distributions). These trends are independent of the smoothing employed, as can be seen in Figure 29, although naturally the range of differential brightness temperatures

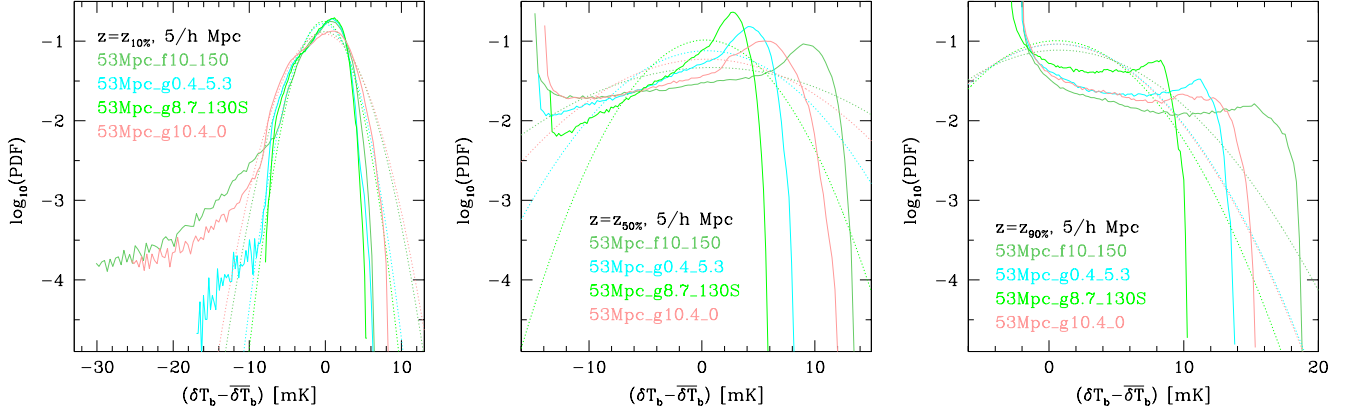


**Figure 29.** Same as in Fig. 28, but for boxcar smoothing of  $5 h^1$  Mpc.

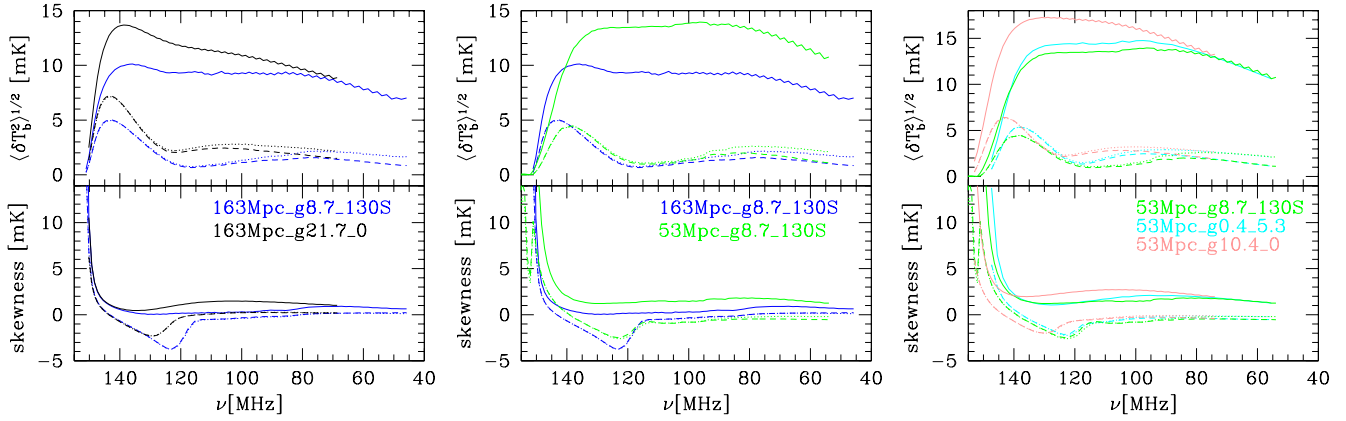


**Figure 30.** (top) The evolution of the rms of the 21-cm fluctuations, and (bottom) evolution of the skewness of the 21-cm PDFs for (left panels) simulations L1 (blue), and L3 (black); (middle panels) simulations L1 (blue) and S1 (green); and (right panels) simulations S1 (green), S4 (cyan) and S5 (light red). Shown are the results at full simulation resolution (solid lines), smoothed with  $3'$  Gaussian beam and 440 kHz bandwidth (dotted lines) and smoothed with a Gaussian beam corresponding to a 2.5km maximum baseline and 440 kHz bandwidth (dashed lines).

is much reduced by the smoothing. The only new feature found in the smoothed data is the non-Gaussian tails for negative  $\delta T_b - \bar{\delta T}_b$  at early times ( $x_m = 0.1$ ). These are result of the H II regions ( $\delta T_b - \bar{\delta T}_b < 0$ ) in the non-self-regulated cases growing relatively large quickly. Consequently, even at these early times their sizes become comparable to the smoothing window size, which results in the non-Gaussian tails. These were not present in the cell-wise PDF distribution, as the individual cells tend to be either fully ionized ( $\delta T_b - \bar{\delta T}_b < -25$  mK) or mostly neutral.

The level of non-Gaussianity of the PDF distributions can, to a first order, be characterized by their skewness, which in turn can be used to distinguish and extract the reionization signals (Harker et al. 2009). In Fig. 30 we show the evolution of the skewness vs. frequency for selected models. We show the skewness for the cell-wise PDF, as well as smoothed with  $3'$  Gaussian beam and 440 kHz bandwidth and smoothed with Gaussian beam corresponding to a 2.5km maximum baseline and 440 kHz bandwidth (bottom panels). Both sets of beam and bandwidth smoothing are roughly as expected for the LOFAR array. We also plotted the rms of the correspondingly-smoothed 21-cm differential brightness temperature fluctuations (top panels). We note that because of the different

beam- and bandwidth smoothing employed here the rms values are slightly different from the ones shown in Figs. 17, 19 and 20.

In all cases, regardless of the specific reionization scenario the skewness evolution for the unsmoothed (1-cell) PDFs follows similar pattern. It stays at a roughly constant, positive value throughout the evolution, until it shoots up just before overlap, very similar to the behaviour observed in Harker et al. (2009). The the beam- and bandwidth-smoothing of the PDFs introduces a significant feature in the skewness, whereby it becomes negative during the intermediate stages of the evolution. Interestingly, this dip of the skewness to negative values closely corresponds to the rise and peak of the differential brightness temperature rms fluctuations, preceding it slightly in time. This feature is universal, observed for every reionization scenario and source model we consider here and suggests an interesting approach for a detection and/or independent confirmation of the rise and peak of the 21-cm rms fluctuations during cosmic reionization.

On the other hand, the skewness of the 21-cm PDF distributions proves to be fairly insensitive to the source model or reionization scenario, resulting in only slight changes in the values. The skewness of the smoothed PDFs also proves largely independent of the box size and resolution and of the details of the interferometer

beam assumptions (i.e. if it is fixed in angular size or evolves with frequency). This suggests that while the feature in the evolution of the skewness is a good indicator of the rise in patchiness, it most likely cannot be used for constraining the properties of the ionizing sources.

## 6 SUMMARY

In this work we have used a large set of cosmological structure formation and reionization simulations in an attempt to gain insight into what can be learned about the properties of the reionization sources based on their observational signatures. In particular, we are interested in determining what observations could be used to discriminate between certain source models, thereby restricting the available parameter space. Here we primarily focused on the redshifted 21-cm signatures, as these can in principle probe the full reionization history and offer a wide range of different probes, from the mean history, through fluctuations measures like rms evolution and power spectra, to PDFs and higher-order statistics which can detect non-Gaussian features.

The observable features of the epoch of reionization derive from the gradual mean transition of the IGM from neutral to highly ionized state, as well as from the patchiness of that transition. The mean transition depends largely on the overall number of ionizing photons emitted by the source per unit time, with some correction due to recombinations which is position-dependent due to density spatial variations. The patchiness, on the other hand depends, in a complicated way on the abundances, clustering and efficiencies of the ionizing sources.

Our structure formation simulations confirm previous results by us and other groups that the high-redshift halo mass functions are inconsistent with either of the widely-used Press-Schechter and Sheth-Tormen analytical fits. In particular, the abundance of rare halos is strongly underestimated by PS, but over-estimated by ST. We find that the nonlinear halo bias is extremely high and very scale-dependent. Linear bias regime is only reached at very large scales,  $k \gtrsim 0.1$ . For the rarest halos ( $3\text{-}\sigma$  and above) linear bias regime is never reached even within our largest, 163 Mpc volume. Therefore, proper account for the nonlinear bias of halos is important and any calculations assuming linear bias are underestimating the halo clustering significantly.

The Jeans mass filtering of low-mass halos in ionized regions and the related self-regulation of reionization results in significantly more extended reionization history and higher integrated electron scattering optical depth (by  $\Delta\tau_{\text{es}} \sim 0.01$ ) compared to the high-mass source-only scenario with the same overlap redshift, albeit both optical depths are still within the current constraints from WMAP. Even more significant are the changes in the reionization geometry, resulting in corresponding differences in the reionization observables. The 21-cm fluctuations are lower at all scales and their PDF distributions are somewhat more Gaussian, although significant non-Gaussianity remains.

In all our simulations reionization occurs inside-out, with the high-density regions being reionized on average earlier than the mean and low-density ones. This inside-out nature of reionization results in the mass-weighted IGM photoionization rates being considerably larger, by factor of a few, than volume-weighted ones. This should always be taken into account as it can easily skew observational measurements depending on the mean density of the regions being probed.

The skewness of the 21-cm PDF distribution smoothed over

LOFAR-like window shows a clear feature correlated with the rise of the rms due to patchiness. This feature does not exist in the unsmoothed data, indicating that it is related to the non-Gaussianity of the large-scale patchy distribution of 21cm emission. The feature exists for any reionization scenario and ionizing source properties and thereby provides a different approach for detecting the rise of large-scale patchiness and an independent check on other detections.

The peak position of the 21-cm rms fluctuations depends significantly on the beam and bandwidth smoothing size as well as on the reionization scenario. As a consequence, it does not always occur at 50% ionization fraction as sometimes is claimed, but instead can happen for ionized fractions as low as 30% and as high as 70%.

The simulation volume has only a modest effect on the results as long as the typical size of the ionized patches is smaller than the volume. However, the fluctuations at large scales (above approximately a fifth of the boxsize) are severely affected. This is especially important at late times, when the ionized patches grow very large. Therefore, at least  $\sim 100/h$  Mpc boxes are required to model the fluctuations during the late stages of reionization.

The ionizing source efficiencies and their correlation properties introduce clear signatures in the reionization observables. As a direct consequence of that, one cannot model low-mass, unresolved sources by simply assigning their emissivity to the resolved higher-mass sources as the latter have abundance which is highly variable over time and different clustering properties from lower-mass sources which provide the bulk of the ionizing photons (see Appendix A).

When self-regulation is present there are only minor differences between the 21-cm observational signatures resulting from high- and low-efficiency ionizing sources, apart from an overall shift of the reionization history. The corresponding PDF distributions are also very similar, which suggests that the source efficiencies in such models can only be constrained by the overall timing of the mean reionization history.

Scenarios where low-mass sources are completely absent, e.g. somehow rendered sterile, are relatively easily distinguishable from the ones where they are present (even if strongly suppressed). On the other hand, our results suggest that numerous low-efficiency sources (case S4) can mimic the effects of suppression (S1). Such scenarios therefore might be difficult to distinguish solely based on power spectra and similar measurements. However, they might still be discriminated through 21-cm PDFs as the no suppression case creates many more high-brightness peaks. Similarly, a high-mass source only scenario (S5) gives quite similar results to the high-efficiency, no suppression case (S3) at the same stages of reionization (albeit these cases overlap at different times for the parameters we have chosen), although they do differ in terms of power at large scales and in number of bright peaks.

The results presented in this work should not be considered to be an ultimate, realistic prediction of the reionization signals. While the assumptions about source efficiencies and suppression we made for our fiducial cases are reasonable based on our current knowledge and likely bracket the realistic range, the uncertainties are still substantial. As more observational data becomes available over time it can be used to restrict the parameter space further and help us refine our theoretical models, which in turn will provide a valuable tool for interpreting the meaning of the observational results in terms of early structure formation, source efficiencies, suppression mechanisms, etc. In this framework our current study, which evaluates in a controlled way the effects of a set of widely different assumptions about the sources of ionizing radiation is a

very useful step towards a more complete understanding of early galaxy formation and feedback.

## ACKNOWLEDGMENTS

ITI was supported by The Southeast Physics Network (SEP-Net) and the Science and Technology Facilities Council grants ST/F002858/1 and ST/I000976/1. This study was supported in part by Swiss National Science Foundation grant 200021-116696/1, Swedish Research Council grant 2009-4088, NSF grants AST-0708176 and AST-1009799, NASA grants NNX07AH09G, NNG04G177G and NNX11AE09G, and Chandra grant SAO TM8-9009X. The authors acknowledge the TeraGrid and the Texas Advanced Computing Center (TACC) at The University of Texas at Austin (URL: <http://www.tacc.utexas.edu>), as well as the Swedish National Infrastructure for Computing (SNIC) resources at HPC2N (Umeå, Sweden) for providing HPC and visualization resources that have contributed to the research results reported within this paper and Partnership for Advanced Computing in Europe (PRACE) grant 2010PA0442 to ITI. KA is supported in part by Basic Science Research Program through the National Research Foundation of Korea (NRF) funded by the Ministry of Education, Science and Technology (MEST; 2009-0068141, 2009-0076868) and by KICOS through K20702020016-07E0200-01610 funded by MOST.

## REFERENCES

- Ahn K., Shapiro P. R., Iliev I. T., Mellema G., Pen U., 2009, *ApJ*, 695, 1430
- Aubert D., Teyssier R., 2010, *ApJ*, 724, 244
- Baek S., di Matteo P., Semelin B., Combes F., Revaz Y., 2009, *A&A*, 495, 389
- Bowman J. D., Rogers A. E. E., 2010, *Nature*, 468, 796
- Ciardi B., Ferrara A., White S. D. M., 2003, *MNRAS*, 344, L7
- Crocce M., Puelblas S., Scoccimarro R., 2006, *MNRAS*, 373, 369
- Cucchiara A., Levan A. J., Fox D. B., Tanvir N. R., Ukwatta T. N., Berger E., Krühler T., Küpcü Yoldaş A., Wu X. F., Toma K., Greiner J., Olivares F. E., Rowlinson A., Amati L., Sakamoto T., Roth K., Stephens A., Fritz A., Fynbo J. P. U., Hjorth J., Male-sani D., Jakobsson P., Wiersema K., O’Brien P. T., Soderberg A. M., Foley R. J., Fruchter A. S., Rhoads J., Rutledge R. E., Schmidt B. P., Dopita M. A., Podsiadlowski P., Willingale R., Wolf C., Kulkarni S. R., D’Avanzo P., 2011, *ApJ*, 736, 7
- Doré O., Holder G., Alvarez M. A., Iliev I. T., Mellema G., Pen U.-L., Shapiro P. R., 2007, *Phys Rev D*, 76, 043002
- Efstathiou G., 1992, *MNRAS*, 256, 43P
- Fernandez E. R., Komatsu E., Iliev I. T., Shapiro P. R., 2010, *ApJ*, 710, 1089
- Field G. B., 1959, *ApJ*, 129, 536
- Friedrich M. M., Mellema G., Alvarez M. A., Shapiro P. R., Iliev I. T., 2011, *MNRAS*, 413, 1353
- Furlanetto S. R., McQuinn M., Hernquist L., 2006a, *MNRAS*, 365, 115
- Furlanetto S. R., Oh S. P., Briggs F. H., 2006b, *Physics Reports*, 433, 181
- Furlanetto S. R., Zaldarriaga M., Hernquist L., 2004, *ApJ*, 613, 1
- Gluscevic V., Barkana R., 2010, *MNRAS*, 408, 2373
- Gnedin N. Y., 2000, *ApJ*, 535, 530
- Gnedin N. Y., Jaffe A. H., 2001, *ApJ*, 551, 3
- Haiman Z., Abel T., Rees M. J., 2000, *ApJ*, 534, 11
- Harker G., Zaroubi S., Bernardi G., Brentjens M. A., de Bruyn A. G., Ciardi B., Jelić V., Koopmans L. V. E., Labropoulos P., Mellema G., Offringa A., Pandey V. N., Pawlik A. H., Schaye J., Thomas R. M., Yatawatta S., 2010, *MNRAS*, 405, 2492
- Harker G. J. A., Zaroubi S., Thomas R. M., Jelić V., Labropoulos P., Mellema G., Iliev I. T., Bernardi G., Brentjens M. A., de Bruyn A. G., Ciardi B., Koopmans L. V. E., Pandey V. N., Pawlik A. H., Schaye J., Yatawatta S., 2009, *MNRAS*, 393, 1449
- Ichikawa K., Barkana R., Iliev I. T., Mellema G., Shapiro P. R., 2010, *MNRAS*, 406, 2521
- Iliev I. T., Ahn K., Koda J., Shapiro P. R., Pen U.-L., 2010, *ArXiv:1005.2502*
- Iliev I. T., et al., 2006, *MNRAS*, 371, 1057
- Iliev I. T., Mellema G., Pen U., Bond J. R., Shapiro P. R., 2008a, *MNRAS*, 384, 863
- Iliev I. T., Mellema G., Pen U.-L., Merz H., Shapiro P. R., Alvarez M. A., 2006, *MNRAS*, 369, 1625
- Iliev I. T., Mellema G., Shapiro P. R., Pen U.-L., 2007a, *MNRAS*, 376, 534
- Iliev I. T., Pen U.-L., Bond J. R., Mellema G., Shapiro P. R., 2007b, *ApJ*, 660, 933
- Iliev I. T., Shapiro P. R., McDonald P., Mellema G., Pen U.-L., 2008b, *MNRAS*, 391, 63
- Iliev I. T., Shapiro P. R., Mellema G., Merz H., Pen U.-L., 2008c, in refereed proceedings of TeraGrid08, *ArXiv e-prints* (0806.2887)
- Iliev I. T., Shapiro P. R., Raga A. C., 2005, *MNRAS*, 361, 405
- Iliev I. T., Whalen D., Mellema G., Ahn K., Baek S., Gnedin N. Y., Kravtsov A. V., Norman M., Raicevic M., Reynolds D. R., Sato D., Shapiro P. R., Semelin B., Smidt J., Susa H., Theuns T., Umemura M., 2009, *MNRAS*, 400, 1283
- Kashikawa N., Shimasaku K., Matsuda Y., Egami E., Jiang L., Nagao T., Ouchi M., Malkan M. A., Hattori T., Ota K., Taniguchi Y., Okamura S., Ly C., Iye M., Furusawa H., Shioya Y., Shibuya T., Ishizaki Y., Toshikawa J., 2011, *ApJ*, 734, 119
- Komatsu E., Smith K. M., Dunkley J., Bennett C. L., Gold B., Hinshaw G., Jarosik N., Larson D., Nolte M. R., Page L., Spergel D. N., Halpern M., Hill R. S., Kogut A., Limon M., Meyer S. S., Odegard N., Tucker G. S., Weiland J. L., Wollack E., Wright E. L., 2011, *ApJS*, 192, 18
- Krug H., Veilleux S., Tilvi V., Malhotra S., Rhoads J., Hibon P., Swaters R., Probst R., Dey A., Dickinson M., Jannuzi B., 2011, *ArXiv e-prints* (ArXiv/1106.6055)
- Larson D., Dunkley J., Hinshaw G., Komatsu E., Nolte M. R., Bennett C. L., Gold B., Halpern M., Hill R. S., Jarosik N., Kogut A., Limon M., Meyer S. S., Odegard N., Page L., Smith K. M., Spergel D. N., Tucker G. S., Weiland J. L., Wollack E., Wright E. L., 2011, *ApJS*, 192, 16
- Lewis A., Challinor A., Lasenby A., 2000, *Astrophys. J.*, 538, 473
- Lonsdale C. J., Cappallo R. J., Morales M. F., Briggs F. H., Benkevitch L., Bowman J. D., Bunton J. D., Burns S., Corey B. E., Desouza L., Doeleman S. S., Derome M., Deshpande A., Gopala M. R., Greenhill L. J., Herne D. E., Hewitt J. N., Kamini P. A., Kasper J. C., Kincaid B. B., Kocz J., Kowald E., Kratzenberg E., Kumar D., Lynch M. J., Madhavi S., Matejek M., Mitchell D. A., Morgan E., Oberoi D., Ord S., Pathikulangara J., Prabu T., Rogers A., Roshi A., Salah J. E., Sault R. J., Shankar N. U., Srivani K. S., Stevens J., Tingay S., Vaccarella A., Waterson M., Wayth R. B., Webster R. L., Whitney A. R., Williams A., Williams C., 2009, *IEEE Proceedings*, 97, 1497
- Lukić Z., Heitmann K., Habib S., Bashinsky S., Ricker P. M., 2007, *ApJ*, 671, 1160

Mao Y., Shapiro P. R., Mellema G., Iliev I. T., Koda J., Ahn K., 2011, ArXiv e-prints

McQuinn M., Lidz A., Zahn O., Dutta S., Hernquist L., Zaldarriaga M., 2007, MNRAS, 377, 1043

Mellema G., Iliev I. T., Alvarez M. A., Shapiro P. R., 2006a, New Astronomy, 11, 374

Mellema G., Iliev I. T., Pen U.-L., Shapiro P. R., 2006b, MNRAS, 372, 679

Merz H., Pen U.-L., Trac H., 2005, New Astronomy, 10, 393

Mesinger A., Dijkstra M., 2008, MNRAS, 390, 1071

Mo H. J., White S. D. M., 1996, MNRAS, 282, 347

Mortlock D. J., Warren S. J., Venemans B. P., Patel M., Hewett P. C., McMahon R. G., Simpson C., Theuns T., González-Solares E. A., Adamson A., Dye S., Hambly N. C., Hirst P., Irwin M. J., Kuiper E., Lawrence A., Röttgering H. J. A., 2011, Nature, 474, 616

Nakamoto T., Umemura M., Susa H., 2001, MNRAS, 321, 593

Navarro J. F., Steinmetz M., 1997, ApJ, 478, 13

Okamoto T., Gao L., Theuns T., 2008, MNRAS, 390, 920

Ouchi M., Shimasaku K., Furusawa H., Saito T., Yoshida M., Akiyama M., Ono Y., Yamada T., Ota K., Kashikawa N., Iye M., Kodama T., Okamura S., Simpson C., Yoshida M., 2010, ApJ, 723, 869

Paciga G., Chang T.-C., Gupta Y., Nityanada R., Odegova J., Pen U.-L., Peterson J. B., Roy J., Sigurdson K., 2011, MNRAS, 413, 1174

Parsons A. R., Backer D. C., Foster G. S., Wright M. C. H., Bradley R. F., Gugliucci N. E., Parashare C. R., Benoit E. E., Aguirre J. E., Jacobs D. C., Carilli C. L., Herne D., Lynch M. J., Manley J. R., Werthimer D. J., 2010, AJ, 139, 1468

Planck Collaboration, Ade P. A. R., Aghanim N., Arnaud M., Ashdown M., Aumont J., Baccigalupi C., Baker M., Balbi A., Banday A. J., et al., 2011, ArXiv e-prints

Press W. H., Schechter P., 1974, ApJ, 187, 425

Quinn T., Katz N., Efstathiou G., 1996, MNRAS, 278, L49

Reed D. S., Bower R., Frenk C. S., Jenkins A., Theuns T., 2007, MNRAS, 374, 2

Ricotti M., Gnedin N. Y., Shull J. M., 2002, ApJ, 575, 33

Rijkhorst E.-J., Plewa T., Dubey A., Mellema G., 2006, A.&A, 452, 907

Salvaterra R., Ciardi B., Ferrara A., Baccigalupi C., 2005, MNRAS, 360, 1063

Shapiro P. R., Giroux M. L., Babul A., 1994, ApJ, 427, 25

Shapiro P. R., Iliev I. T., Raga A. C., 2004, MNRAS, 348, 753

Shaver P. A., Windhorst R. A., Madau P., de Bruyn A. G., 1999, A.&A, 345, 380

Sheth R. K., Tormen G., 2002, MNRAS, 329, 61

Shin M.-S., Trac H., Cen R., 2008, ApJ, 681, 756

Sokasian A., Abel T., Hernquist L., Springel V., 2003, MNRAS, 344, 607

Susa H., Umemura M., 2004, ApJL, 610, L5

Thomas R. M., Zaroubi S., Ciardi B., Pawlik A. H., Labropoulos P., Jelić V., Bernardi G., Brentjens M. A., de Bruyn A. G., Harker G. J. A., Koopmans L. V. E., Mellema G., Pandey V. N., Schaye J., Yatawatta S., 2009, MNRAS, 393, 32

Trac H., Cen R., 2007, ApJ, 671, 1

Zahn O., Mesinger A., McQuinn M., Trac H., Cen R., Hernquist L. E., 2011, MNRAS, 414, 727

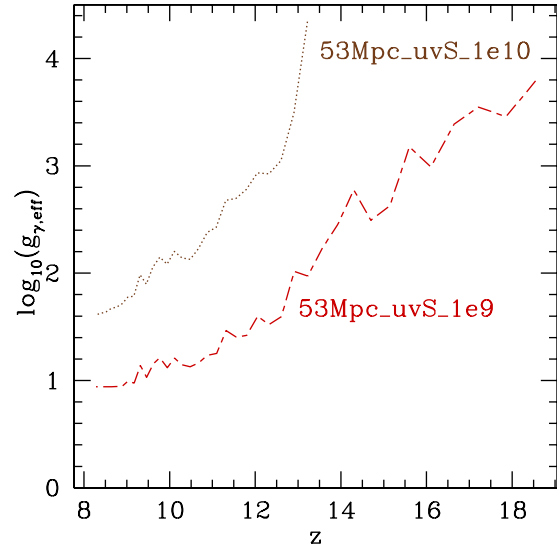


**Figure A1.** Effective efficiency factors  $g_\gamma$  vs. redshift for simulations S8 and S9, defined so as to ensure the same total number of ionizing photons emitted per atom as in our fiducial simulation, S1.

#### APPENDIX A: REIONIZATION BY RARE, MASSIVE, VARIABLE-LUMINOSITY SOURCES

Simulations 53Mpc\_uvS\_1e9 and 53Mpc\_uvS\_1e10 (S8 and S9 in Table 2) are investigating the effects of keeping the global, volume-averaged emissivity of ionizing photons per unit time fixed at each redshift, while raising the minimum source mass, assumed to be  $10^9 M_\odot$  for S8 and  $10^{10} M_\odot$  for S9. The overall number of photons emitted at each timestep are set to be exactly equal, at all times, to the one yielded by our fiducial case, S1. The resulting effective efficiencies  $g_\gamma$  are shown in Figure A1. Simulation S8 has the same high-mass halo population as our fiducial simulation, but no active low-mass sources (LMACHs) at all. Therefore, the effective efficiencies start very high, at several thousand photons per atom, as the relatively few high-mass sources at early time have to ‘compensate’ for the more numerous low-mass sources present in the fiducial case which are missing here, as well as for all photons emitted before  $z \sim 19$  in our fiducial simulation, during which time there are no active sources larger than  $10^9 M_\odot$ . However, as the number of high-mass sources rises exponentially,  $g_{\gamma,eff}$  drops precipitously, to less than 40 by  $z = 12.6$  and less than 20 by  $z = 11$ . Towards overlap  $g_{\gamma,eff}$  settles on  $\sim 8.7$ , the value adopted in our fiducial case, as by then all low-mass sources are suppressed and the high-mass sources are identical to the ones in the fiducial case. Note that although in this case the sources belong to the same halos as in S5 and overlap is reached at a similar redshift, this S8 case is different in assuming the same step-by-step total emissivity as in our fiducial case, L1, which naturally makes them variable in time, unlike case L5 discussed before, which had a fixed photon emissivity per unit halo mass.

Case S9 is still more extreme, since only quite massive halos, with masses above  $10^{10} M_\odot$  are allowed to be active sources. The first such massive halos form in our simulation only at  $z = 13.2$  and they remain relatively rare ( $\sim 3 - \sigma$ ) even at overlap ( $z = 8.2$ ). As a consequence, their effective efficiency is very high at all times, starting at over 20,000 and reaching  $\sim 40$  at overlap. In order to avoid hyper-luminous sources during the first timestep, we



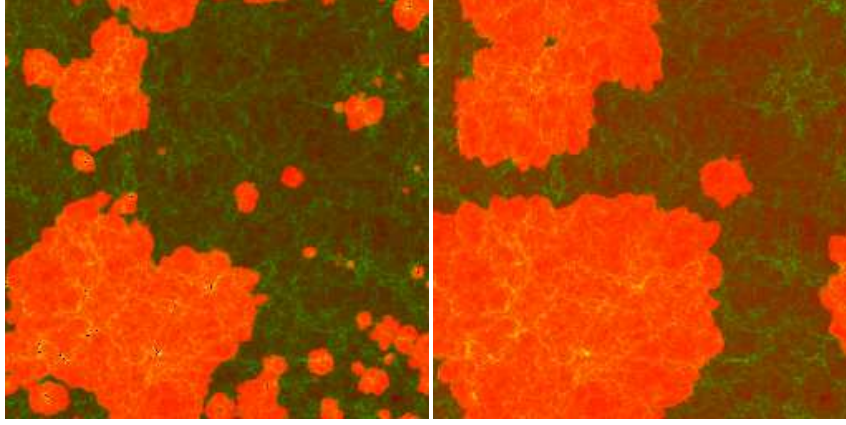


**Figure A2.** Spatial slices of the ionized and neutral gas density from our radiative transfer simulations with boxsize 53 Mpc at box-averaged ionized fraction by mass  $x_m \sim 0.50$ . Shown are the density field (green) overlaid with the ionized fraction (red/orange/yellow) and the cells containing sources (dark/blue). Shown are cases S8 and S9.

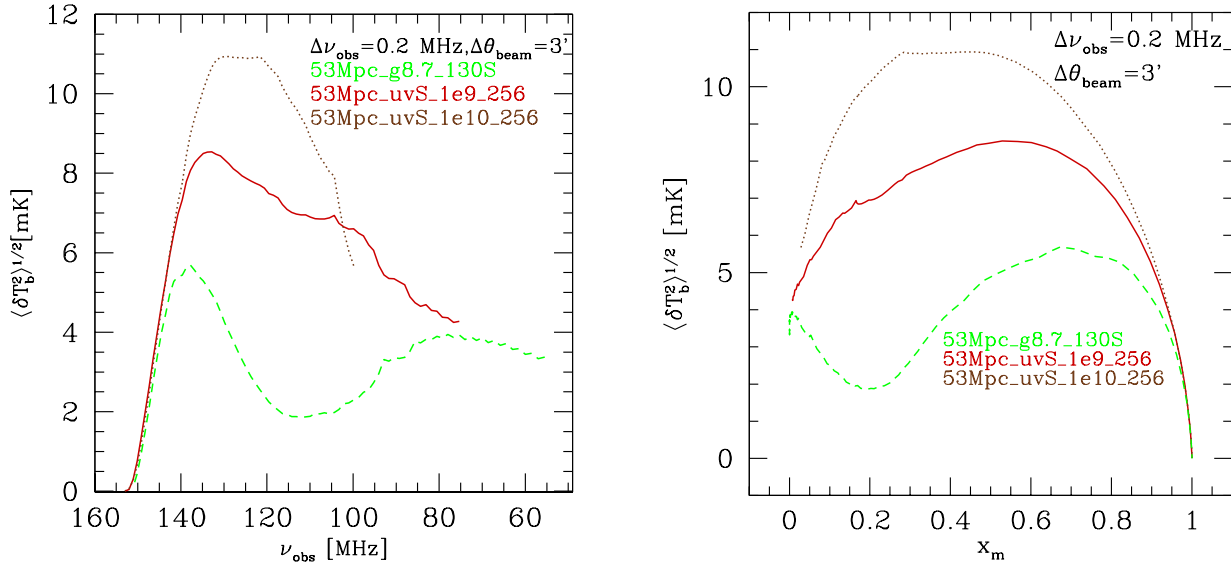


**Figure A3.** The evolution of the rms fluctuations of the 21-cm background, for beamsizes  $3'$  and bandwidth 0.2 MHz and boxcar filter vs. frequency (left) and vs. mean mass-weighted ionized fraction (right). Shown are simulations S1 (green, short dashed), S8 (dark red, long dash-short dash) and S9 (brown, dotted).

distributed the photons that were emitted at  $z > 13.2$  in the fiducial case over the first several timesteps of run S9. Clearly, both S8 and S9 scenarios are not very realistic physically, given this vast range of change in the source efficiencies.

Since in cases S8 and S9 we imposed the same global integrated ionizing photon emissivities per timestep as in our fiducial case S1 (but higher minimum source mass), the averaged global reionization histories of those two cases closely follow the one of the fiducial simulation once the first haloes above the respective minimum cutoff form in our volume. The only remaining difference is that at early times ( $z > 11$ ) the ionized fraction in case S9 is a little lower than in the other two cases, as a consequence of our imposition of a bit more gradual initial release of photons in this case, in order to avoid hyper-luminous sources, as explained above. However, unlike S1, both simulations S8 and S9 yield  $x_m/x_v \approx 1$ , since in those latter cases the ionized patches produced by the few,

luminous sources present are far less correlated with the underlying density field (Fig. A3). This is a consequence of the I-fronts quickly escaping into the nearby voids, which compensates for the exponential rise of the number of ionizing sources forming at the high density peaks (although we note that even in this case reionization remains inside-out, as the ionized regions are still over-dense on average). This results in H II region distributions which are clearly distinct from the rest. As the cutoff mass increases, there are exponentially fewer ionizing sources, which consequently are much more efficient (cf. Fig. A1). Hence, those hyper-luminous sources produce correspondingly large H II regions, which are less correlated with the underlying density field and are more spherical than in the other cases, as they are produced by few, but highly clustered sources.

This distinct H II region geometry of cases S8 and S9 also yields very characteristic 21-cm signatures. The massive, rare,



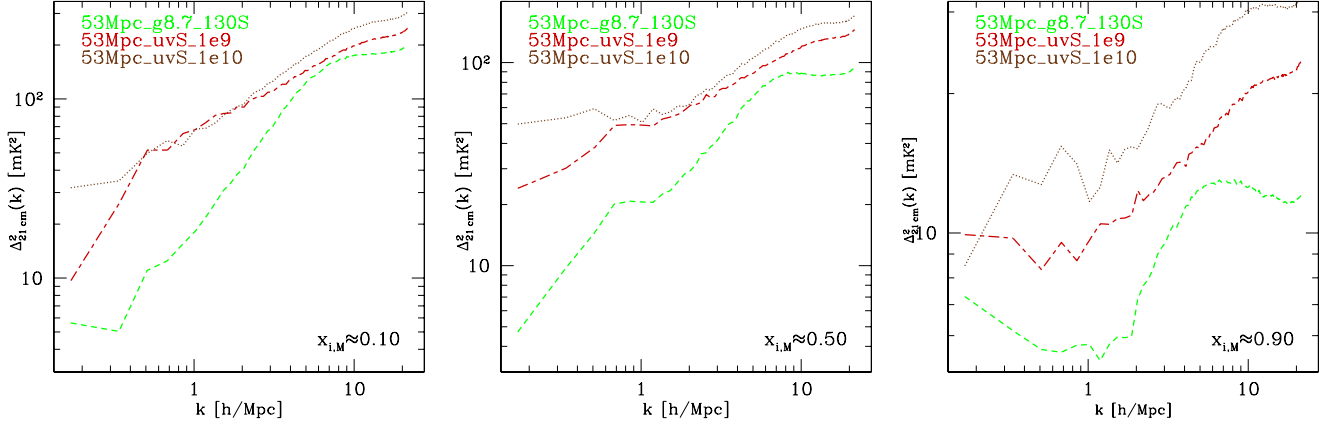


**Figure A4.** 21-cm differential brightness temperature fluctuation power spectra for varying source models. Shown are the epochs at which the ionized fractions are (left)  $x_m = 0.1$ , (middle)  $x_m = 0.5$  and (right)  $x_m = 0.9$ . All cases are labelled by color and line-type, as follows: S1 (green, short-dashed), S8 (dark red, long dash-short dash) and S9 (brown, dotted).

highly efficient sources quickly produce very large H II regions and thus high rms fluctuations at large scales and a very broad peak, with an almost constant value ( $\langle \delta T_b^2 \rangle^{1/2} = 10.39 - 10.94$ ) for a wide range of mean ionized fractions by mass,  $x_m = 0.21 - 0.58$ . There is also no initial dip of the rms fluctuations, which normally occurs when the highest density peaks are ionized, but the H II regions are still much smaller than the smoothing beam size. In models S8 and S9 the ionized patches grow so fast that their typical sizes are of order or large than the beam at all times. Such a scenario therefore yields a signal which is both stronger and quite different from the others. The results for the lower minimum source mass cutoff case with same reionization history, S8, show similar properties to S9, namely a broad and relatively high rms peak and no initial dip. However, the peak value in this case, at  $\sim 8$  mK, is noticeably lower than for model S9 ( $\sim 11$  mK) and is more similar to the typical values for the majority of cases ( $\sim 5 - 8$  mK). The corresponding PDF distributions (not shown) are noticeably wider, with a long non-Gaussian tail at high differential brightness temperatures ( $\delta T_b - \bar{\delta T}_b > 30 - 40$  mK) than in the fiducial self-regulation case, S1.

The corresponding 21-cm power spectra (Figure A4) for cases S8 and S9 also show significantly higher signal on all scales compared to our fiducial case S1. During the early stages of reionization the power at large scales ( $k \lesssim 0.4$  h/Mpc) for S9 is almost an order of magnitude higher than for S1. During the late stages the difference decreases considerably, but still remains  $\sim 2$  on large ( $k < 2$  h/Mpc), as well as very small ( $k > 8$  h/Mpc) scales. As could be expected, the case with lower minimum mass, S8, is intermediate between S1 and S9, but much closer to S9 throughout the evolution.

Our scenario S9 is similar to the high minimum source mass case, S4, considered in McQuinn et al. (2007). These authors set the minimum source mass to  $4 \times 10^{10} M_\odot$ , somewhat higher than in S9. Their ionizing photon production is similarly set to reproduce, step-by-step, the one of their fiducial case. Their results are qualitatively similar to what we find. The rare, efficient and strongly clustered sources yielded 21-cm power spectra which were higher and flatter than in their fiducial case, with the difference decreasing over time (cf. Fig. 17 in McQuinn et al. 2007). However, some quantitative differences remain, due to the somewhat different approach we have taken, as well as some numerical and resolution

differences. Apart from the higher source mass cutoff adopted by McQuinn et al. (2007), which results in a stronger source bias, other important differences include lower resolution of their N-body and radiative transfer simulations, and lack of Jeans mass filtering. Unlike our high-resolution simulations, which resolve all atomically-cooling halos ( $M > 10^8 M_\odot$ ), the N-body structure formation simulations used by McQuinn et al. (2007) resolved only halos with mass above  $10^9 M_\odot$ , with lower-mass sources included in some cases by sub-grid modelling. More importantly, their fiducial case (whose photon production per timestep was the basis for their high-mass cutoff case S4) yielded late overlap and included no Jeans mass filtering (several of their other simulations included it, but not this one). Therefore, their photon production per unit source mass was necessarily very low, making their fiducial case more similar to our low-efficiency case S4 than to our fiducial simulation S1. Finally, we take account of peculiar velocity when calculating more precise 21-cm power spectra (including redshift space distortions) (Mao et al. 2011). Despite these differences, our results agree reasonably well on a qualitative level.

We note that models S8 and S9 are rather unrealistic, as they assume unphysically high and time-variable luminosities, as well as the suppression of all sources with mass below  $10^{10} M_\odot$  (or, less aggressively,  $10^9 M_\odot$  for case S8), for which no clear mechanism exists. We have included these models here primarily in order to demonstrate, under controlled circumstances, the effect of higher source-mass cutoff on the 21-cm observables. Such a higher source cutoff mass occurs numerically in simulations with large volumes and limited dynamic range (e.g. Baek et al. 2009; Thomas et al. 2009), and, therefore, it is important to evaluate the level of reliability of such models. Our results show that including only the high-mass sources can result in over-estimating the 21-cm rms fluctuations by up to a factor of 2, while  $P(k)$  at small  $k$  where the first generation of observations will probe, could be over-estimated by as much as an order of magnitude at the 50% ionized epoch. It can also yield quite a different evolution, even for the same boxsize, numerical resolution and the same integrated photon emissivity over time. One should therefore be aware of these potential pitfalls and adjust their modelling accordingly. A better simulation approach would be to add the lower-mass, unresolved sources by sub-grid modelling.

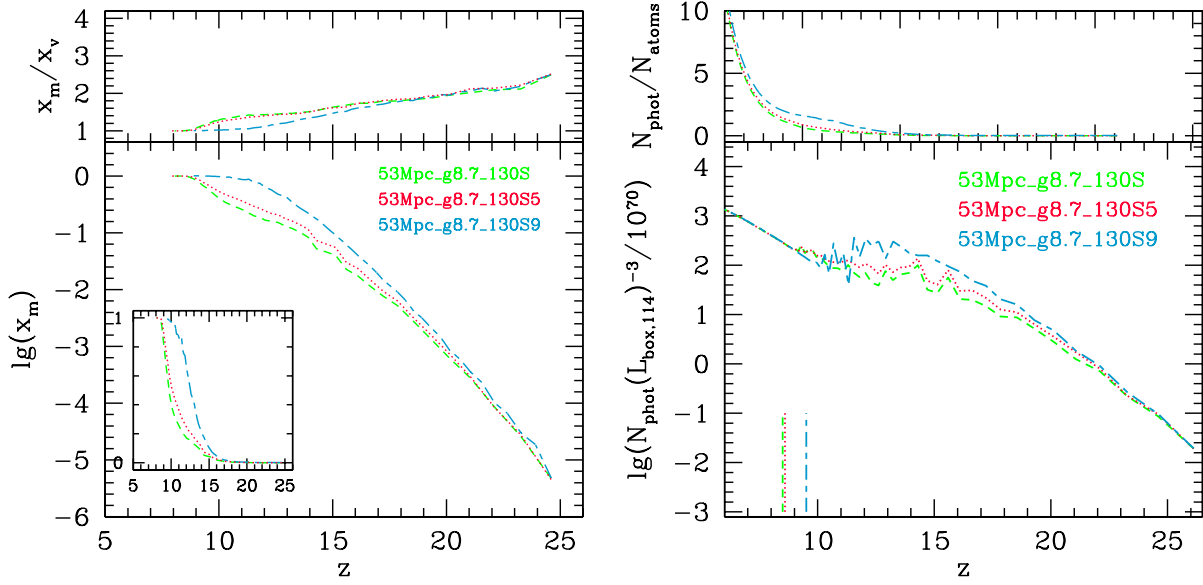


**Figure A5.** (left) (bottom panel) Mass-weighted reionization histories for cases S1, S6 and S7, each with different Jeans mass filtering threshold. (top panel) Ratio of the corresponding mean mass-weighted and volume ionized fractions,  $x_m/x_v$ . (bottom panels) Number of ionizing photons emitted by all active sources (thick lines) in the computational volume per timestep and (top panels) cumulative number of photons per total gas atom released into the IGM. Vertical lines mark the overlap redshift in each case. All curves on both left and right are labelled by color and line-type, as follows: S1 (green, short-dashed), S6 (light blue, long dash-short dash) and S7 (red, dotted).

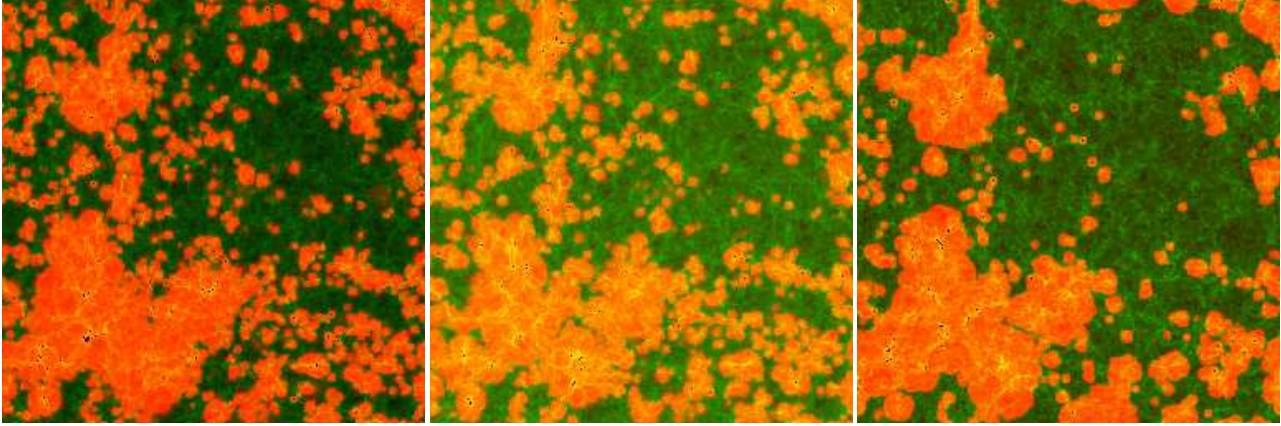


**Figure B1.** Spatial slices of the ionized and neutral gas density from our radiative transfer simulations with boxsize  $37 h^{-1} \text{ Mpc}$ , all at box-averaged ionized fraction by mass  $x_m \sim 0.50$ . Shown are the density field (green) overlaid with the ionized fraction (red/orange/yellow) and the cells containing sources (dark/blue). Shown are cases S1, S7, and S6.

## APPENDIX B: DEPENDENCE ON THE JEANS SUPPRESSION THRESHOLD

Here we consider variations of our source suppression threshold, with the goal establishing the robustness and validity of our fiducial model, S1, where we use  $x_{\text{threshold}} = 0.1$ . We have ran two additional models, S6 and S7, whereby we raise this ionization threshold for low-mass source suppression to  $x_{\text{threshold}} = 0.9$  and  $0.5$ , respectively. In our fiducial case the suppression criterion for partially-ionized cells is more aggressive than in these new cases. The reasonable value to be adopted for this suppression threshold is still quite uncertain at present, thus it is important to check the sensitivity of our results to variations in its value. In fact, it is most likely that a sharp on-off condition like this is an oversimplification and in reality the suppression boundary is gradual, with full sup-

pression of the smallest galaxies, partial one for intermediate-mass galaxies, up to no suppression at all for sufficiently massive galaxies. However, given the current uncertainties, the range of possible suppression models is very large and it is difficult to fully explore numerically. Instead, we have chosen to consider three very different cases covering the full range of the threshold value, in order to evaluate the effect of these uncertainties on the reionization history and observables. We note, however, that we consider our original source suppression criterion to be well motivated, for the following reasons. Although for numerical reasons our suppression criterion is defined in terms of ionized fraction, physically it is related to the temperature state of the IGM, for which the ionization state is used as a proxy. When a given region is photoionized, its temperature rises to  $\sim 10^4 \text{ K}$ , with the exact value dependent on the intensity

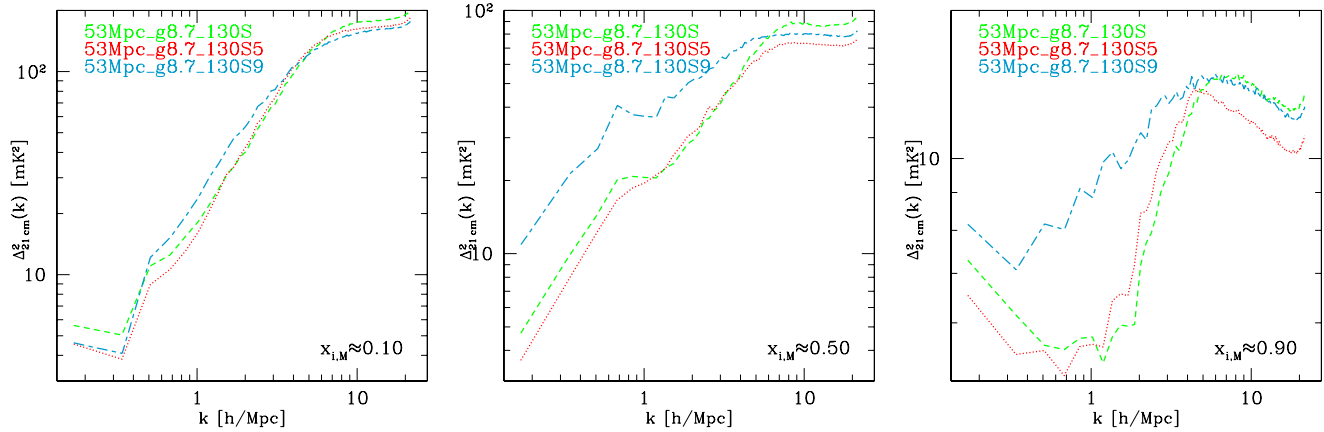


**Figure B2.** 21-cm differential brightness temperature fluctuation power spectra for varying source models. Shown are the epochs at which the ionized fractions are (left)  $x_m = 0.1$ , (middle)  $x_m = 0.5$  and (right)  $x_m = 0.9$ . All cases are labelled by color and line-type, as follows: S1 (green, short-dashed), S6 (light blue, long dash-short dash) and S7 (red, dotted).

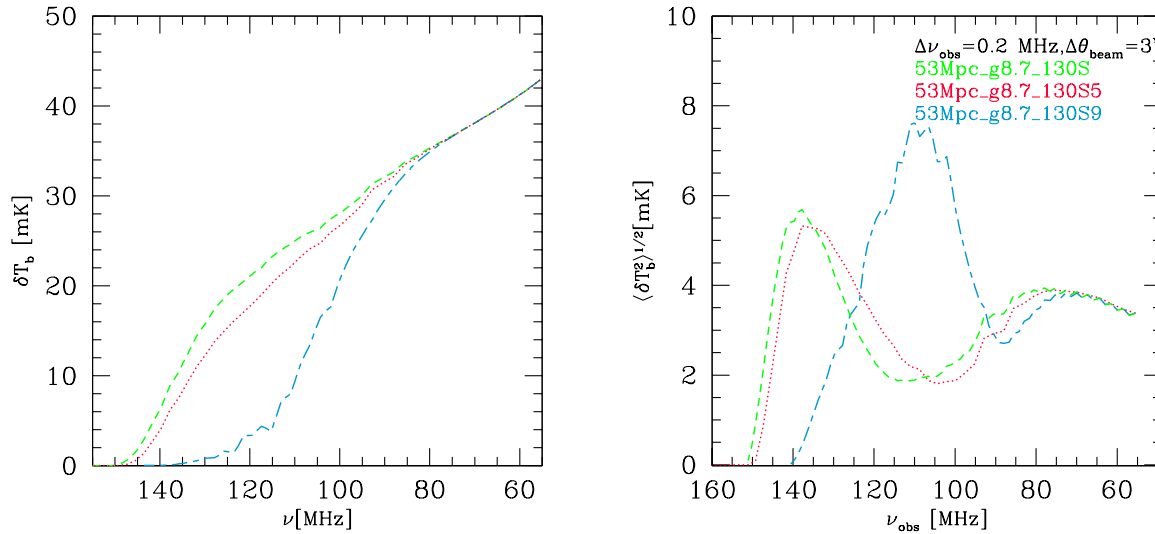


**Figure B3.** The evolution of the mean 21-cm background (left) and its rms fluctuations for Gaussian beams size  $3'$  and bandwidth 0.2 MHz and boxcar frequency filter (right) vs. observed 21-cm frequency. Shown are simulations (green, short-dashed), S6 (light blue, long dash-short dash) and S7 (red, dotted).

and spectrum of the ionizing radiation, ranging from  $\sim 20,000$  K for Pop. II stellar spectra and QSO's to  $\sim 30,000 - 40,000$  K for Pop. III (Shapiro et al. 2004). This rises the gas pressure and thus the Jeans mass, to  $10^9 M_\odot$  or more. In order for the low-mass halos to be able to re-form in a previously-ionized region its temperature should decrease to well below  $10^4$  K. However, in the mostly metal-free gas during these early epochs there is no efficient radiative coolant available and therefore the main cooling mechanisms are the local adiabatic expansion and Compton scattering of CMB photons. Since both of these processes are relatively slow and inefficient we expect that our fiducial more aggressive ionized fraction-based source suppression criterion is more physically realistic than the milder suppression of the new cases. However, given the significant uncertainties of the Jeans filtering process, which can only be properly modelled by hydrodynamical simulations with detailed

and realistic microphysics, we consider all of these very different suppression criteria and study their consequences below.

The reionization histories and cumulative numbers of ionizing photons emitted derived for the three suppression criteria are shown in Figure A5 (left). Clearly, only a very weak suppression ( $x_{\text{threshold}} = 0.9$ , case S7) yields any significant differences. Compared to our fiducial case S1, many fewer low-mass sources are suppressed in S7, and of these a significant fraction are allowed to become active again shortly after suppression (since in absence of radiation recombinations quickly bring the neutral fraction back up above 10%). The evolution of the number of photons produced in simulation S6 is up to  $\sim 2$  higher in the middle stages of reionization, while the corresponding number for S7 is essentially the same as in S1 throughout the evolution.

The Jeans mass filtering nonetheless still has a significant effect, keeping the ionized fraction well below the corresponding one

for the no-suppression case S3 (cf. Fig. 9, right panels). Eventually, the fully-ionized fraction of the volume becomes sufficiently large to suppress almost all low-mass sources even with this mild suppression criterion and the reionization process slows down until sufficient number of massive sources form and are able to finish this process and reach overlap. In contrast, the intermediate case, S7 ( $x_{\text{threshold}} = 0.5$ ) shows only modest differences from the fiducial model S1, manifesting themselves mostly in bringing reionization forward by  $\Delta z \sim 0.4$ , compared to  $\Delta z \sim 1.2 - 3.2$ , and very different shape of the reionization history for case S6. Similarly, the integrated electron-scattering optical depth for the mild suppression case S6 is  $\tau_{\text{es}} = 0.111$ , much higher than in the fiducial case ( $\tau_{\text{es}} = 0.080$ ), while for the intermediate suppression case the increase is much more modest, at  $\tau_{\text{es}} = 0.089$ . The cumulative number of photons per atom at overlap,  $\sim 2$ , is very similar in all three cases.

The variations in the geometry of reionization (Fig. B1) are mostly found in the small-scale structures. There are significantly fewer such structures in the weak suppression case S6. The merged H II regions are typically slightly larger, as well as rounder and with smoother boundaries compared to the fiducial simulation S1. Once again the intermediate case S7 is very similar to S1, with only minor differences in small-scale features. These visual impressions are further confirmed by comparing the 21-cm power spectra (Figure B2). The weak suppression case S6 has significantly more power at intermediate and large scales ( $k \lesssim 5$ ) during all stages of reionization, more so at late times, but less power on small scales than our fiducial case S1. On the other hand, the intermediate model S7 matches S1 fairly closely, except for having less power on very small scales.

The 21-cm mean differential brightness temperature (Fig. B3, left) for the weak suppression case S7 shows an initial steep decline around  $\nu \sim 100$  MHz, followed by a sudden change of slope at  $\nu \sim 125$  MHz and a very slow decrease thereafter. This behaviour is quite different from models S1 and S6 (which again follow almost identical evolution), as well as from all other models discussed earlier. The only model with a similarly sharp decrease of the mean brightness temperature is the high efficiency, no suppression case S3, which however does not have the same long slow evolution tail at late times due to lack of suppression.

Finally, the differential brightness temperature rms fluctuations (Fig. B3, right) for the weak suppression case, S6, peak much earlier, at  $\nu \approx 110$  MHz (but still significantly later than the no suppression case S3, which underlines the importance of even a very weak low-mass source suppression) reaching  $\langle \delta T_b^2 \rangle^{1/2} \approx 8$  mK. Uniquely, this model exhibits a very long tail of slow decline of the rms fluctuations beyond the peak. This is related to its very different (and, as we argued earlier, possibly less physically realistic) suppression model. Case S6 also exhibits significant fluctuations in the differential brightness temperature fluctuations, once again indicating that this suppression model might be less physically realistic than our standard suppression model. The intermediate suppression model S6 follows the same evolution as the fiducial case S1, but shifted to slightly earlier time.

In summary, all results prove fairly insensitive to the precise value of the Jeans suppression threshold assumed, as long as it is not at the very weak suppression limit. Both  $x_{\text{threshold}} = 0.1$  and  $0.5$  yield essentially the same evolution, apart from a slight offset in time. On the other hand, a very high suppression threshold ( $x_{\text{threshold}} = 0.9$ , i.e. weak suppression) results in a very different (and somewhat unstable) evolution with several characteristic observational signatures. We have, however, argued above that such a

weak suppression is likely less realistic physically. Our suppression model therefore proves quite robust to a threshold variation within the plausible range.